3 From Basic Physical Properties of InAs/InP Quantum Dots to State-of-the-Art Lasers for 1.55 μm Optical Communications

An Overview

Jacky Even, Cheng Wang, and Frédéric Grillot

CONTENTS

3.1 Introduction 95
3.1.1 Toward InP-Based Quantum Dot Lasers for Optical Telecommunications 95
3.1.2 Lasers on (311)B InP Substrate 97
3.1.3 Lasers on (100)InP Substrate 98
3.1.4 Current Status of the Dynamic Performance of InP-Based Qdot Laser 99
3.2 Basic Physical Properties of Buried InAs/InP Quantum Dots 101
3.2.1 Quantum Dot Electronic Structure 101
3.2.2 Carrier Scattering Processes in Quantum Dot 103
3.2.3 Gain, Refractive Index, and Line-Width Enhancement Factor 104
3.3 Free-Running Quantum Dot Lasers 107
3.3.1 Amplitude Modulation Response 107
3.3.2 Line-Width Enhancement Factor (α-Factor) 111
3.3.3 Impacts of Carrier Capture and Relaxation Processes 116
3.4 Conclusion 119
Acknowledgments 120
References 120

3.1 INTRODUCTION

3.1.1 Toward InP-Based Quantum Dot Lasers for Optical Telecommunications

Semiconductor lasers play a crucial role in optical data communication and telecommunication applications. Nowadays, high-definition television, video on demand, broadband internet, and mobile phones are available all around the globe. The exponential rise in cost-effective information transmission would not have been possible without the introduction of optical transmission systems, which in turn are enabled by semiconductor lasers. A hundred million new semiconductor lasers are deployed in communication systems every year, generating several billion dollars of annual revenue at the component level [1]. Higher performance semiconductor laser sources are in strong

K13633_C003.indd 95 4/4/2016 4:17:31 PM

demand because of the increasing data traffic in the WAN (wide area network), MAN (metropolitan area network), and LAN (local area network), which drives the development of novel semiconductor laser technologies.

Since the first demonstration of a semiconductor laser in 1962, the field has been witnessing the development from bulk-structure lasers and quantum-well (Qwell) to the advanced nanostructure quantum wire (Qwire), quantum dash (Qdash), and quantum dot (Qdot) lasers. In the 1960s, the bulk laser was developed on the basis of semiconductor heterostructures, which provided efficient confinement of charged carriers in the active region [2]. In particular, the double heterostructure (DH), which also yields optical confinement, has transformed semiconductor lasers from the laboratory to industry [3]. Quantum confinement occurs when one or more spatial dimensions of a nanocrystal approach the de Broglie wavelength of the carrier (on the order of 10 nm). The confinement of carriers leads to the quantization of the density of states, and splits the energy band of bulk semiconductors into energetic subbands [4]. In the 1970s, the first Qwell laser, in which carriers are confined in one dimension, was demonstrated [5]. Its recognized advantages over DH lasers were the reduced threshold current by decreasing the thickness of the active layer and the tunability of the wavelength via changing the Qwell thickness.

Increase of the confinement dimension leads to Qwire (2D confinement), Qdash (quasi-3D confinement), or Qdot structures (3D confinement). The 3D spatial confinement of Qdots results in an atomic-like density of states. The concept of Qdot semiconductor was proposed by Arakawa and Sakaki in 1982 [6], predicting temperature independence of the threshold current. Thereafter, reduction in threshold current density, high spectral purity, enhancement of differential gain, and chirp-free properties were theoretically discussed in the 1980s [7]. The most straightforward technique to produce an array of Qdots is to fabricate suitably sized mesa-etched quantum wells grown by metal-organic chemical vapor deposition (MOCVD) or molecular beam epitaxy (MBE). However, nonradiative defects produced during the etching procedure leads to a degradation of the material quality, which results in unsuitable structures for lasers. In the 1990s, both selective growth and self-assembled growth technique, which can avoid nonradiative defects, were well developed. Particularly, the Stranski–Krastanov growth mode turned out to be very successful for InGaAs/GaAs systems [8,9]. The strain-induced self-organization of InGaAs/GaAs quantum dots [10,11] yields threshold current densities as low as ~60 A cm^{-2} at room temperature [12]. Extensive work on the GaAs-based Qdot system has been carried out, which resulted in tremendous improvement in laser performance [13]. An ultralow threshold current density of 17 A cm^{-2} and a high output power of 7 W were achieved in InAs/GaAs lasers [14,15]. Nowadays, the InAs/GaAs Qdot products have already become commercially available in the market [8,16]. Meanwhile, several self-assembled growth techniques, such as solid-state MBE [17], gas-source MBE [18], MOVPE [19], and chemical-beam epitaxy (CBE) [20], have been improved and successfully used to grow Qdot materials.

Nevertheless, the GaAs-based Qdot laser devices emit usually in the O band (1260–1360 nm) of the telecommunication windows and are hardly able to reach the desirable long-haul communication window of ~1.55 μm. Instead, the InAs active region grown on InP substrates allows the realization of laser devices working in the C band window (1530–1565 nm) because of the smaller lattice mismatch. In the current market, InP-based 1.55 μm Qwell laser devices have shown substantial improvement in the optical characteristics in comparison with their DH counterparts. In order to improve the Qwell laser performance, InAs dots grown on InP substrates have attracted much attention in the research field. However, the formation of nanostructures on InP is much more challenging than on the GaAs substrate [21]. Although the InAs/InP and the InAs/GaAs systems have the same material in the dots, they differ in three aspects: (a) lattice mismatch in InAs/InP (~3%) is smaller than that in InAs/GaAs (~7%); (b) InAs/InP dots exhibit less confinement potential for electrons, but a stronger confinement for holes; (c) InAs/InP material shares the same cation (In), while the InAs/GaAs shares the same anion (As) at the interface [22]. The small lattice mismatch and the complex strain distribution can result in the formation of a new class of self-assembled Qdash nanostructures instead of Qdots. These are elongated, dot-like structures exhibiting interesting

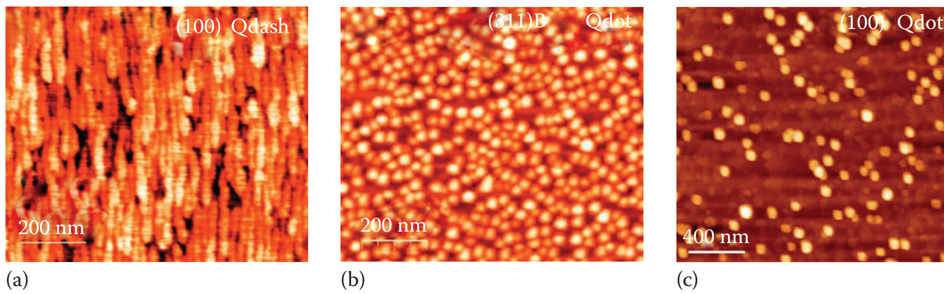

FIGURE 3.1 AFM image of InAs/InP (a) Qdashes on (100) orientation substrate, (b) Qdots on (311)B substrate, and (c) Qdots on (100) substrate. (a: From Zhou, D. et al., *Appl. Phys. Lett.*, 93, 161104, 2008; b: From Zhou, D. et al., *Appl. Phys. Lett.*, 93, 161104, 2008; c: From Bertru, N. et al., Two-dimensional ordering of self-assembled InAs quantum dots grown on (311)B InP substrate, *Proceedings of SPIE, Quantum Sensing and Nanophotonic Devices VII*, Vol. 7608, p. 76081B, 2010.)

mixed characteristics in between those of the Qwell and the Qdot [23]. Strongly anisotropic QDash nanostructures are even closer to Qwire in their electronic properties of [24]. Therefore, realization of real InAs/InP Qdots requires specific epitaxial growth procedures. This is done by employing conventional or miscut (100) InP substrates as well as (311) InP misoriented substrates along with various innovations in the growth process [25]. Nevertheless, reduction of the dot size and suppression of the size dispersion due to the self-assembly growth procedure are still challenges in achieving high-quality epitaxial material and hence better device performance. Currently, the size dispersions, characterized by the photoluminescence (PL) line width in terms of the full-width at half-maximum (FWHM), are ~20 meV at 10 K for Qdots and ~50 meV at room temperature for Qdashes [26–29] and Qdots [30]. Further improvements in material quality are still required for them to be competitive with the mature InAs/GaAs Qdot systems. InAs dots formed on the (100) InP substrate usually have a low dot density (on the order of 10^9–10^{10} cm^{-2}) [31]. These laser structures usually require multiple stacked layers for sufficient material gain. In contrast, dots grown on high-index (311)B substrates can lead to a large increase of the Qdots density, commonly in the 5×10^{10}–10^{11} cm^{-2} range [32,33]. Figure 3.1 shows the atomic force microscopy (AFM) images of (a) InAs/InP Qdash, (b) Qdots on a (311)B substrate, and (c) Qdots on a (100) substrate. The first InAs/InP Qdot laser was reported by Ustinov et al. in 1998 [34,35], which emitted at ~1.9 μm at 77 K. Room-temperature operation was realized soon [36]. In the following, we review the development of InAs/InP Qdot lasers on both (311)B and (100)InP substrates employing the InAs/InGaAsP or InAs/InGaAlAs active material regions.

3.1.2 Lasers on (311)B InP Substrate

High-indexed (311)B InP substrates can offer a high density of nucleation points for the Qdot islands, which strongly reduces surface migration effects and leads to the formation of more symmetric Qdots in the planar direction. As a result, high density and uniform distribution of Qdots can be obtained. Many studies have been carried out on the InP (311)B substrate, and a relatively high density of 5–13 × 10^{10} cm^{-2} has been realized [36,38]. The inhomogeneous line-width broadening due to Qdot size dispersion can be constrained within 50 meV by using the double-capping-layer technique [30,39]. Figure 3.2a presents the AFM image of a typical InAs/InP dot on a (311)B substrate. The Qdot base resembles a circle rather than a square with a typical size of 30–50 nm in diameter, and the height for this kind of dot with cylindrical symmetry is usually several nanometers [33]. The cross-sectional scanning tunneling microscopy (X-STM) image of the Qdot structure in Figure 3.2b shows a truncated, faceted profile of the Qdot.

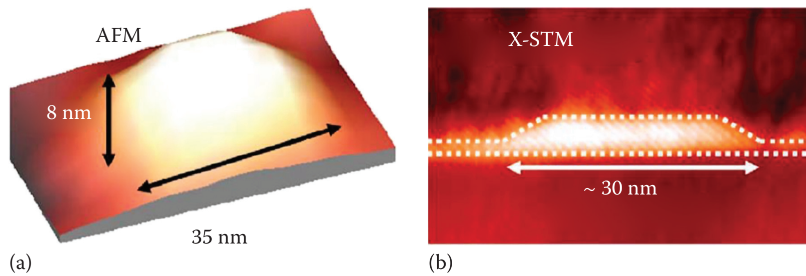

FIGURE 3.2 Structural investigations on InAs/InP Qdots on (311)B-oriented substrate. (a) AFM image: the bright areas represent the top of the Qdot; (b) X-STM image: the bright areas represent the rich InAs areas. (From Cornet, C. et al., *Phys. Rev. B*, 74, 035312, 2006.)

Using the InAs/InGaAsP active region, Nishi et al. demonstrated a Qdot laser with seven stacking layers grown by MBE [36]. The laser device had a dot density of 2×10^{10} cm^{-2} and a threshold current density of 4.8 kA cm^{-2}, and emitted at 1.4 μm at room temperature. By using a double-capping technique, Caroff et al. achieved a high dot density of 1.1×10^{11} cm^{-2}, emitting close to 1.55 μm at room temperature [40]. The laser had a high modal gain of 7 cm^{-1} per dot layer. The threshold current density and transparency current density were 190 A cm^{-2} (63 A cm^{-2} per layer) and 68 A cm^{-2} (23 A cm^{-2} per layer), respectively. These are the best threshold performances reported in this material system. Homeyer et al. reported a broad-area laser emitting at 1.54 μm at room temperature with a record internal quantum efficiency of 62% [41]. The laser consisted of only two stack layers with a modal gain of 8 cm^{-1} per layer. The dot density was also as high as $\sim 1.0 \times 10^{11}$ cm^{-2}. A single-active-layer laser device with a gain of 13 cm^{-1} was demonstrated in 2007, but it lased only up to 295 K [32]. Recently, a low-internal-loss laser of 6 cm^{-1} was reported, which included nine stack layers with a total modal gain of 25 cm^{-1} [42]. However, the InAs/InGaAsP material system usually has poor temperature stability with a characteristic temperature of only 25–50 K at room temperature due to the low conduction band offset [25].

By employing the InAs/InGaAlAs active region, Saito et al. first demonstrated a Qdot laser at the wavelength of 1.63 μm; the threshold current density was 660 A cm^{-2} (132 A cm^{-2} per layer) [43]. The extracted internal loss was 3.6 cm^{-1}, which is the lowest reported value for any InAs/InP system. Six years later, by exploiting the Al atoms in the spacer layers and employing the strain compensation technique, Akahane et al. demonstrated a 30-stack-layer laser with a threshold current density of 2.7 kA cm^{-2} (90 A cm^{-2} per layer) [44]. Subsequently, with improvement in the material growth quality, the threshold current density of the 30-stack laser was reduced to 1.72 kA cm^{-2} (57.4 A cm^{-2} per layer) with extremely high temperature stability. The characteristic temperature (T_0) was 114 K (20°C–75°C), which further improved to a record 148 K (25°C–80°C) in a 20-stack laser [45]. However, the laser had a high internal loss of ~26 cm^{-1} due to the imperfect coupling of the optical mode with the multistack gain medium.

3.1.3 Lasers on (100)InP Substrate

The formation of self-assembled Qdot on the (100)InP substrate is more complicated. The formation of the dot or dash strongly depends on the growth conditions and the thickness of InAs layers. The major problem in obtaining good performance of the laser is the low dot density on this kind of substrate.

In the InAs/InGaAsP material system, the growth of dots is mostly based on CBE or MOCVD techniques. Allen et al. reported a Qdot laser using the CBE technique, which was operated in pulsed mode at room temperature [46]. The pulsed threshold current density was 3.56 kA cm^{-2} (713 A cm^{-2} per layer), where a dot height trimming procedure with growth interruptions was

employed. The dot density was increased by using the higher energy barrier to 3–6 × 10^{10} cm^{-2}. On the other hand, Lelarge et al. used a hybrid growth technique with an MBE-grown active region in conjunction with MOCVD grown p-doped cladding and contact layers [47]. The continuous wave (CW) threshold current density was 1.4 kA cm^{-2} (240 A cm^{-2} per layer) and T_0 was 56 K at room temperature. Particularly, the laser showed a very high modal gain of 64 cm^{-1} (10.7 cm^{-1} per layer). The laser grown by MOCVD showed a reduced threshold current density of 615 A cm^{-2} (123 A cm^{-2} per layer) [48]. The transparency current density was as low as 30 A cm^{-2} and the internal loss was only 4.2 cm^{-1}.

In the InAs/InGaAlAs material system, Kim et al. first demonstrated a Qdot laser using an assisted growth technique of a thin gas underlying layer before the growth of InAs dots in the InGaAlAs matrix [49,50]. The achieved dot density was 6.0 × 10^{10} cm^{-2}, and the laser exhibited a threshold current density of 2.8 kA cm^{-2} (400 A cm^{-2} per layer). The measured T_0 was 377 K for temperatures up to 200 K, and 138 K above 200 K. More recently, Gilfert et al. reported a high-gain Qdot laser using the MBE method [51]. A low internal loss of 4 cm^{-1} and a high gain of 15 cm^{-1} per layer were reported. The lasing threshold current density was 1.95 kA cm^{-2} (325 A cm^{-2} per layer).

Very recently, Mollet et al. reported a very high modal gain of 97 cm^{-1} for an InAs/InP(100) Qdash laser. However, the internal loss was also as high as 23 cm^{-1} [52]. Generally, the performance of InAs/InP lasers has improved significantly since its first demonstration. However, it still needs improvement to be comparable with InAs/GaAs laser devices.

AQ2

3.1.4 Current Status of the Dynamic Performance of InP-Based Qdot Laser

In fiber-optic links, the laser transmitter may be either directly modulated, known as directly modulated (DM) laser, or externally modulated using a modulator. In the direct modulation scheme, the driving current carries the transmitted data and is directly applied to the laser. In the external modulation scheme, the laser, which is subjected to a constant bias current, emits a continuous wave, while an external modulator switches the optical power on or off according to the data stream. In the external modulation scheme, electrooptic (EO) or electroabsorption (EA) modulators are commonly used [53]. EO modulators, such as the Mach–Zehnder modulator, utilizes a signal-controlled crystalline material exhibiting the EO effect (Pockels effect) to modulate the CW laser light. The EO effect is the change in the refractive index of the material resulting from the application of a DC or low-frequency electric field. The EA modulator controls the intensity of a laser beam via an electric voltage. Its operation can be based on the Franz–Keldysh effect [54], that is, a change in the absorption spectrum caused by an applied electric field, which changes the bandgap energy but usually does not involve the excitation of carriers by the electric field. However, most EA modulators are made in the form of a waveguide with electrodes for applying an electric field in a direction perpendicular to the modulated light beam. For achieving a high extinction ratio, one usually exploits the quantum-confined Stark effect, which describes the effect of an external electric field upon the light absorption spectrum or emission spectrum of a quantum-well structure. Both EO and EA modulators are operated at a few volts (below 10 V). In comparison with EO modulators, EA modulators have the convenient feature that they can be integrated with the laser on a single chip to create a data transmitter in the form of a photonic integrated circuit [55,56].

In contrast, DM lasers are the most common, particularly for short-reach systems. They have the lowest cost and the least energy consumption, but they usually suffer the chirp characteristics [68]. DM lasers generally produce more chirps for higher extinction ratios, leading to an optimum setting for trading off the signal-to-noise ratio and chirp penalty. Aiming to realize chirp-free DM laser devices, many attempts have been made to develop nanostructured semiconductor lasers. Table 3.1 summarizes the reported dynamic performance of InP-based Qdot and Qdash lasers in the literature, including the modulation bandwidth and the α-factor, which is linked to the frequency chirp under direct modulation.

TABLE 3.1
Dynamic Characteristics of Qdot and Qdash Lasers Grown on InP Substrate

References	Material	Bandwidth	α-Factor, $\leq I_{th}$	α-Factor, $>I_{th}$	Differential Gain, Gain Compression
[57]	Qdot, (311)B	4.8 GHz	~1.8	~6	7.3×10^{-15} cm^2 6.4×10^{-16} cm^3
[58]	Qdot, (100)	5 GHz 15 Gbps			
[59]	Qdot, (100)	9 GHz 22 Gbps			
[60]	Qdot, (100) p-doped and tunnel injection	14.4 GHz	~0		0.8×10^{-15} cm^2 5.4×10^{-17} cm^3
[61]	Qdash, (100)	7.6 GHz			
[62]	Qdash, (100)	6 GHz @ undoped 8 GHz @ p-doped 12 GHz @ p-doped and tunnel injection	~1 @ p-doped ~0 @ p-doped and tunnel injection		
[63]	Qdash, (100) p-doping	8 GHz			
[64]	Qdash, (100)	9.6 GHz 10 Gbps		5–7	
[65]	Qdash, (100) p-doped	10 GHz			1.1×10^{-15} cm^2
[66]	Qdash, (100)	10 GHz 20 Gbps			
[67]	Qdash, (100) p-doped	10 Gbps		2.2	
[52]	Qdash, (100)	~10 GHz		~5 @ undoped ~2.7 @ p-doped	$1–2 \times 10^{-15}$ cm^2

Martinez et al. reported a Qdot laser grown on the (311)B InP substrate with a modulation bandwidth of 4.8 GHz. The above-threshold α-factor was high (~6) and did not significantly depend on the bias current [57]. However, most reported dynamics of 1.55 μm lasers are for nanostructures grown on (100)InP substrates. Gready et al. demonstrated an InAs/InGaAlAs/InP Qdot laser with a 3 dB bandwidth of 5 GHz [58]. Interestingly, the laser showed a much larger signal modulation capability: 15 Gbps at 4 dB extinction ratio. The discrepancy between the small- and large-signal performances was attributed to the large nonlinear gain compression effect [69]. By optimizing the barrier width and the number of stack layers, the performance of the structure was improved by the same group. The small-signal modulation bandwidth was increased to 9 GHz, and the large signal modulation was operated up to 22 Gbps with an extinction ratio of 3 dB [59]. The best performance of InAs/InP Qdot laser was achieved by Bhowmick et al. recently [60]. The laser material system was InAs/InGaAlAs, and the active zone was grown on the (100)InP substrate. Tunnel injection and p-doping techniques enhanced the modulation bandwidth up to 14.4 GHz, and a near-zero α-factor was realized in this structure. For Qdash lasers on the (100)InP substrate, most works employed the p-doping technique to improve the modulation bandwidth and to reduce the α-factor [52,62,67,70]. Mi et al. showed that the modulation bandwidth could be increased from 6 GHz for the undoped

laser to 8 GHz with the p-doped laser [62]. Mollet et al. demonstrated that the α-factor could be reduced from 5 down to 2.7 by p-doping [52]. On the other hand, the tunnel injection technique further increased the modulation bandwidth to more than 10 GHz while reducing the α-factor to near zero [60,62]. Consequently, a low chirp of 0.06 nm at a modulation frequency of 8 GHz was achieved in the Qdash laser and the same chirp level at 10 GHz in the Qdot laser.

3.2 BASIC PHYSICAL PROPERTIES OF BURIED InAs/InP QUANTUM DOTS

3.2.1 Quantum Dot Electronic Structure

Schematically, the active region of a Qdot laser often consists of a 3D separate confinement heterostructure (SCH, also known as barrier), a 2D carrier reservoir (RS, roughly corresponding to the wetting layer), and dots spatially confined in three dimensions. Figure 3.3 shows an illustration of the electronic structure in a Qdot laser.

Carriers in the barrier and the wetting layer can be treated as quasi-free particles. Thus, quasi-continuum electronic states are formed in the SCH and the RS. The total densities of states for the SCH (per volume) and that for the RS (per area) are, respectively, given by [71]

$$\rho_{SCH} = 2\left(2\frac{m_{SCH}^*}{\hbar^2}\pi k_B T\right)^{3/2} \quad (3.1)$$

$$\rho_{RS} = \frac{m_{RS}^*}{\pi\hbar^2}k_B T \quad (3.2)$$

with m^* the effective mass of either electrons or holes. The quasi-continuum carrier reservoir coupling with the localized energy states of the dots results in smaller energy separations and thus overlapping states at higher energies [72]. The discrete states lying at lower energies are separated by a few tens of millielectronvolts in the conduction band (CB), while it is smaller in the valence band (VB) due to higher effective hole mass.

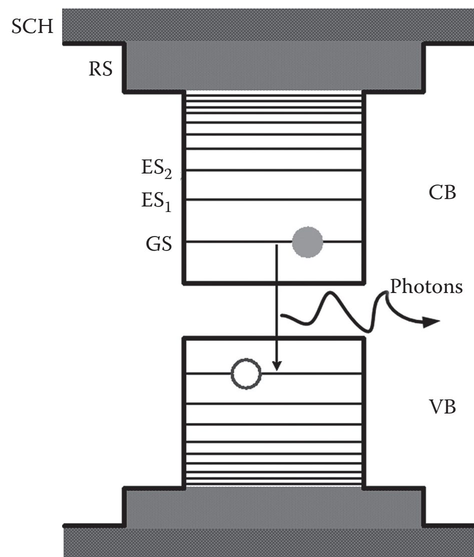

FIGURE 3.3 Schematic of a QD laser electronic band structure of electrons and holes.

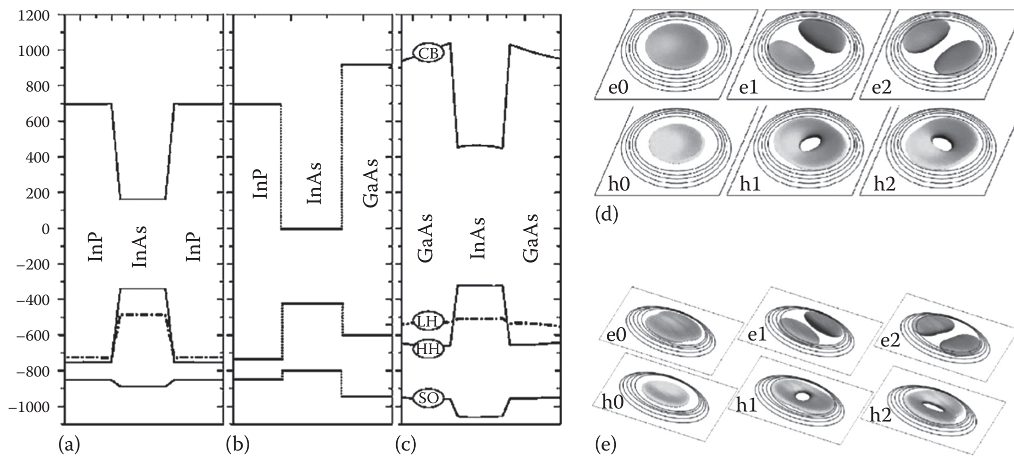

FIGURE 3.4 Vertical scan through the confinement potential for an InAs Qdot embedded in (a) InP and (b) GaAs. (c) The energetic positions of the unstrained band edges for InP and GaAs relative to InAs. Wave function representations for electrons and holes for the first InAs/InP Qdot states (d) on (100) substrate and (e) on (311)B substrate, with a Qdot height of 2.93 nm. e0, e1, and e2 stand for electronic states, and h0, h1, and h2 stand for hole states. The (311)B substrate induces an anisotropy of the wave function. (From Cornet, C. et al., *Phys. Rev. B*, 74, 035312, 2006.)

Accurate simulation of the electronic structure of an InAs/InP quantum dot can be performed using multiband $\mathbf{k}\cdot\mathbf{p}$ theory including strain and piezoelectric effects [73]. Based on the eight-band $\mathbf{k}\cdot\mathbf{p}$ theory, Figure 3.4a through c shows the confinement potential of the InAs/InP Qdot in comparison with the InAs/GaAs Qdot system [33]. In the absence of strain (Figure 3.4b), the band edge of InP is different from that of GaAs relative to the active material InAs. InP confines the holes more strongly, whereas GaAs does the same for the electrons. In the presence of strain, the band-edge energies are altered as shown in Figure 3.4a for InAs/InP and in Figure 3.4c for InAs/GaAs, by mainly hydrostatic strain in the conduction band and biaxial strain in the valence band. Consequently, the heavy/light hole degeneracy is lifted at the Γ point. The change of band edge for InAs embedded in GaAs is stronger because of the larger lattice mismatch (6.6% compared to only 3.1% for InP). The most striking feature is the smaller (strained) bandgap of InAs in InP than in GaAs, which enables the former to reach the 1.55 μm emission, which is hard to achieve for InAs/GaAs Qdots. Figure 3.4a and c show that the depth of the electron confinement potential is similar in both systems, and therefore one can expect a comparable spectrum for confined electron states provided the Qdots share the same morphological properties. However, this does not hold for hole states since the confinement potential for InAs/InP Qdots is much deeper and the heavy–light hole splitting is smaller. Figure 3.4d and e illustrate the first three electron and hole wave functions (70% isosurface) of a single particle for both (100) (Figure 3.4d) and (311)B InP (Figure 3.4e) substrates, which is obtained by solving the Schrödinger equation. The symbols e0 and h0 stand for 1Se and 1Sh states, and e1, e2, and h1, h2 stand for 1Pe and 1Ph states. The single-particle states provide a basis for the configuration interaction model, which can be applied to calculate the excitonic properties, including correlation and exchange. Finally, the excitonic optical absorption spectra can be computed; the details can be found in [33].

Because of the Coulomb interaction, electrons and holes in the semiconductor can be bound into electron–hole pairs, known as *excitons*. The distance between the electron and the hole within an exciton is called the Bohr radius of the exciton. Typical exciton Bohr radius of semiconductors is a few nanometers [74]. The exciton's nature can be modified by the confinement structure, and thus it can exhibit different optical properties. The assumption holds as long as the electron and hole populations do not show significant deviations. Such a simplified picture was capable of describing the basic optical properties.

K13633_C003.indd 102 4/4/2016 4:17:48 PM

3.2.2 Carrier Scattering Processes in Quantum Dot

In a Qdot device, once the current injection generates charge carriers in the 3D barrier, the carriers will be transported into the 2D RS, which acts as a carrier reservoir for the localized discrete Qdot states. The carrier capture process refers to the subsequent carrier capture from the RS to the ESs of the dots. In the dots, the carriers relax from high energetic ESs down to the GS level. Finally, radiative recombination of electrons and holes takes place and lasing occurs often on the GS. These processes are well reflected by the time-resolved photoluminescence (TRPL) of an InAs/InP Qdot device, as shown in Figure 3.5a. The spectra are fitted with three Gaussian peaks, which, respectively, correspond to the Qdot excitonic GS at 0.94 eV, the first Qdot ES at 0.99 eV, and the RS ~1.05 eV. The peak of the spectra shifts from RS at 10 ps via ES at 600 ps toward GS at 1500 ps with time evolution after the optical excitation [75]. In addition, carrier capture directly from the RS into the GS is also possible. This direct channel accelerates the carrier indirect process (via ES) to the lasing GS, and plays an important role on the dual (GS and ES) lasing process, as pointed out in InAs/InP Qdot lasers [76]. Moreover, those electronic states also exhibit inter-dot electronic coupling [72]. As in Qwell lasers, the carrier transport process plays an important role in determining the Qdot laser's dynamics as well, which induces a parasitic-like roll-off that is indistinguishable from an RC roll-off in the modulation response, and thus limits the modulation bandwidth [77,78]. TPRL shows that the carrier transport time across barrier to the RS is several picoseconds (1–5 ps) depending on the thickness of the SCH layer [79,80]. The carrier capture and relaxation transition processes are supported mainly by two physical mechanisms: Coulomb-interaction-induced carrier–carrier scattering (Auger process), and carrier–LO phonon scattering. The scattering behavior is different at low and high excitation carrier densities. At low excitation density, the carrier interaction with LO phonons can provide efficient scattering channels provided that energy conservation is fulfilled. While the energy separation of Qdot states typically does not match the LO phonon energy, this scattering mechanism is often possible for holes due to their dense states [81]. The carrier–LO phonon scattering process is found to be temperature-dependent: high temperature accelerates this scattering rate [82,83]. When a high-density carrier plasma is created in the carrier reservoir, carrier–carrier scattering accounts for the efficient capture from the RS into the localized Qdot states as well as the relaxation between

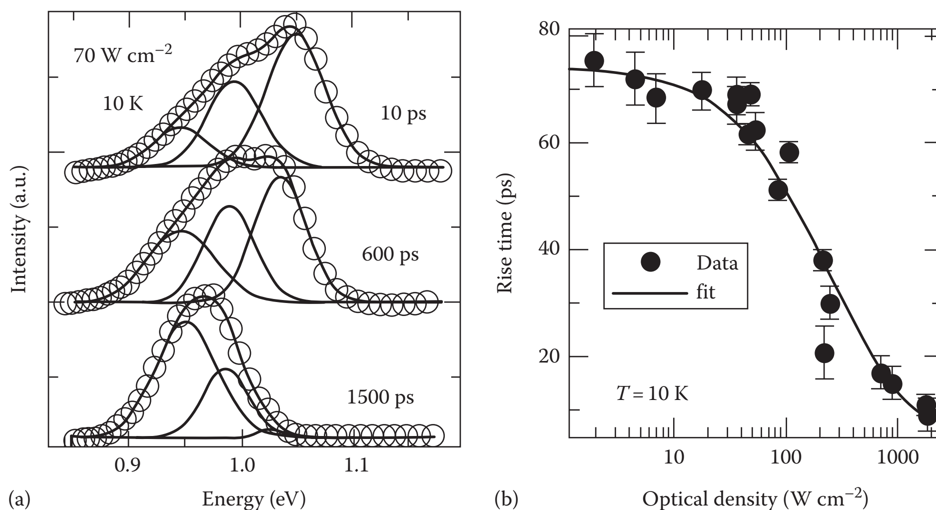

FIGURE 3.5 (a) TRPL spectra recorded at 10 K for 10, 600 and 1500 ps after the optical excitation at 790 nm with an optical excitation density of 70 W cm^{-2}. Spectra are fitted with three Gaussian curves. (b) TRPL analysis of the rise time of the Qdot as a function of the excitation intensity at 10 K. (a: From Miska, P. et al., *Appl. Phys. Lett.*, 92, 191103, 2008; b: From Miska, P. et al., *Appl. Phys. Lett.*, 94, 061916, 2009.)

the discrete Qdot states [84]. Auger scattering can be categorized into three types according to the initial electronic states of the carriers involved. One type involves two carriers in the RS states [85]; another type is with one carrier in an ES state while the other in the RS [86]; and the third type has both carrier occupied the ES [87]. In contrast to the carrier–phonon interaction process, the Auger process is carrier-density-dependent, as shown in Figure 3.5b [88]. At 10 K, the carrier relaxation time into the GS of the Qdots reduces from ~75 ps under an optical excitation of 1 W cm^{-2} down to about 10 ps for an excitation density of 2000 W cm^{-2}.

From the analysis of TRPL rise time of Qdot devices, both the capture and relaxation times are found to vary over a wide range from 1 up to 100 ps depending on the excitation intensity [82,89]. However, for a moderate RS carrier density of 10^{11}–10^{12} cm^{-2}, the typical carrier scattering times are on the order of 1–10 ps [79,90]. For the processes related to Coulomb many-body interactions, relaxation within the Qdot is typically on a faster timescale than the carrier capture from the RS into the Qdot. Processes involving holes are typically faster than the corresponding processes involving electrons, and capture to the excited states is faster than capture to the ground states. Hence in a dynamical scenario, first the holes are captured to the excited Qdot states and immediately scattered via relaxation to the Qdot ground states. Capture of electrons is somewhat slower; the subsequent relaxation for electrons is only slightly slower than for holes [81].

From the aspect of rate equation modeling of Qdot lasers, carrier distributions in all states are usually assumed to be under the quasi-equilibrium condition with Fermi–Dirac distribution, which is suitable for sufficiently rapid intraband relaxation processes [91]. Carrier occupations, at least in the GS and in the RS, must be modeled in order to distinguish the Qdot laser from the Qwell laser. However, for achieving moderate accuracy and correlating with experimental data in the InAs/InP Qdot system, it is necessary to consider the population in the first ES, which can have significant influence on the laser's static and dynamic characteristics. Inclusion of more states would be more accurate but at a price of losing simplicity as well as the intuitive physical image.

Rigorous calculation of carrier scattering rates is a stiff task, which requires sophisticated many-body quantum theory that treats intraband collision processes. In [91–93], a phenomenological formula was proposed to take into account the carrier-dependent capture and relaxation time in a semiempirical model:

$$\tau_i = \frac{1}{A_i + C_i N_{RS}} \tag{3.3}$$

where

i denotes the capture or relaxation process
A_i is the phonon-assisted scattering rate
C_i is the coefficient determining the Auger-assisted scattering by carriers in the RS (N_{RS})

Although this expression leads to good agreement with the TRPL experiments in [75], parameters A_i and C_i can be quite different from device to device [76], thereby limiting the applicability of this expression. Because of the fact that once the laser is operated above threshold there is a large density of carriers in the RS, which does not vary much with the bias current, it is a reasonable approximation to assume the carrier scattering time as constant, which simplifies the rate equation model for the study of Qdot laser dynamics.

3.2.3 Gain, Refractive Index, and Line-Width Enhancement Factor

The laser field and the semiconductor gain medium are coupled by the gain and the carrier-induced refractive index, or equivalently, by the complex optical susceptibility. To determine these quantities, it is necessary to solve the quantum mechanical gain medium equations of motion for the microscopic polarization. In principle, these dynamical equations should be derived using the

K13633_C003.indd 104 4/4/2016 4:17:50 PM

full system Hamiltonian, which includes contributions from the kinetic energies, the many-body Coulomb interactions, the electric–dipole interaction between the carriers and the laser field, as well as the interactions between the carriers and phonons. The effects of injection current pumping should also be included [92].

The connection between the classical electrodynamics and quantum mechanics is effected through the macroscopic polarization P and the microscopic polarization p_α:

$$P = \frac{1}{V}\sum_{\alpha} \mu_\alpha p_\alpha \tag{3.4}$$

In Qdot lasers, the processes include the GS, ES, RS, and barrier transitions. V is the active region volume, and the polarization summation is performed over all interband optical transitions. The complex optical susceptibility is connected with the polarization via

$$\chi = \frac{1}{\varepsilon_0 n_b^2}\frac{P}{E} \tag{3.5}$$

where ε_0 and E are the vacuum permittivity of light and the amplitude of the electric field, respectively. The gain g and the carrier-induced refractive index δn in the model are defined by

$$\frac{d}{dt}E(t) = \Gamma_p \frac{cg}{2n_b}E(t) + j\frac{\omega\delta n}{n_b}E(t) \tag{3.6}$$

where

ω and c are the laser frequency and the velocity of light, respectively

n_b is the refractive index

Γ_p is the optical confinement factor

We can obtain the following relation between the gain, refractive index, susceptibility, and the polarization [94]:

$$g = -\frac{\omega n_b}{c}\mathrm{Im}\{\chi\} = -\frac{\omega}{\varepsilon_0 n_b c}\frac{\mathrm{Im}\{P\}}{E} \tag{3.7}$$

$$\delta n = \frac{n_b}{2}\mathrm{Re}\{\chi\} = \frac{1}{2\varepsilon_0 n_b}\frac{\mathrm{Re}\{P\}}{E} \tag{3.8}$$

Introducing the differential gain a, the phenomenological gain can be expressed as

$$g = a(N - N_{tr}) \tag{3.9}$$

with N and N_{tr} being the injected carrier density and transparency carrier density of zero gain, respectively.

In semiconductor lasers, the nonlinear gain phenomenon plays an important role in both static and dynamic characteristics such as spectral properties, modulation bandwidth, and frequency chirping [95]. The main physical mechanisms behind nonlinear gain are attributed to the spectral hole-burning, spatial hole-burning, and carrier heating [96,97]. Furthermore, the gain nonlinearity was found to enhance the quantum confinement of carriers and carrier relaxation processes [98].

Spectral hole-burning is the formation of a dip in the gain spectrum due to stimulated emission. The dip occurs by the recombination of electrons and holes at a specific energy and the subsequent redistribution of carrier energies due to carrier–carrier scattering. The scattering process takes place on the timescale of the order of 50–100 fs and leads to a dip width of about 20–40 meV. It also ensures that temperature equilibrium is established among the carriers within the same timescale. Carrier heating is related to the fact that the carrier temperatures can be different from the lattice temperature due to the stimulated emission and free-carrier absorption [96]. The carrier temperatures relax toward the lattice temperature by electron–phonon scattering processes within a timescale of 0.5–1 ps. The nonlinear gain effect is usually characterized by a phenomenological gain compression factor, as

$$g_{nl} = \frac{g}{1+\xi S} \approx g(1-\xi S) \tag{3.10}$$

with S being the photon density. This expression shows that the linear gain g is reduced at high power density.

The refractive index change related to the optical interband transition as expressed in Equation 3.8 is known as *anomalous dispersion* [99]. Another important contribution to the index change is the free-carrier plasma originating from intraband transitions [100]. In Qwell lasers, this contribution to the differential index is well described by the Drude model [101]:

$$\delta n_{fc} = -\frac{\Gamma_p e^2 N}{2 n_b \varepsilon_0 m^* \omega^2} \tag{3.11}$$

with e the electronic charge. Analogous transitions in Qdot lasers can be envisaged between bound Qdot states and the continuum levels of the RS and the barrier. It has been shown that the Drude formula can also be applied to the case of Qdot lasers when the Qdot carriers are not tightly confined and when working at photon energies in the 0.8–1.0 eV region [100].

In semiconductor lasers, it is well known that any change in the imaginary part of the susceptibility (gain) will be accompanied by a corresponding change in its real part (refractive index) via the Kramers–Kronig relations. The line-width enhancement factor (or α-factor) describes the coupling between the carrier-induced variation of real and imaginary parts of susceptibility, and is defined as [102]

$$\alpha_H = \frac{\partial\,\mathrm{Re}\{\chi\}/\partial N}{\partial\,\mathrm{Im}\{\chi\}/\partial N} \tag{3.12}$$

Employing Equations 3.7 and 3.8, the above definition is equivalent to the following often-used expression:

$$\alpha_H = -2\frac{\omega}{c}\frac{\partial n/\partial N}{\partial g/\partial N} \tag{3.13}$$

In a practical case, the variation of the carrier concentration is usually small, which justifies taking the derivatives at the operating point and assuming a linear dependence of $g(N)$ and $n(N)$. Equation 3.13 can therefore be written as

$$\alpha_H = -2\frac{\omega}{c}\frac{\Delta n}{\Delta g} \tag{3.14}$$

Through the relation between the refractive index and frequency variation, we can obtain the following equivalent formula:

$$\alpha_H = 2\frac{n_b}{c}\frac{\Delta\omega}{\Delta g} \tag{3.15}$$

The α-factor plays a crucial role in driving fundamental features of semiconductor lasers such as the spectral line-width broadening [103], frequency chirp [104], mode stability [105], and nonlinear dynamics subject to optical injection [106] or optical feedback [107–109]. Typical Qwell lasers often exhibit α-factor values in the order of 2–5 [78]. For Qdot lasers, earlier analyses have suggested a zero or near-zero α-factor due to the delta-function-like discrete density of states. A symmetrical gain curve indeed leads to a dispersive curve of the refractive index with a zero value at the gain peak. However, experimental α-factor values in Qdot lasers vary over a wide range from zero up to more than 10, but a giant value (as high as 60) was also reported [110–112]. The nonzero α-factor is attributed to the large inhomogeneous broadening, the off-resonant bound and continuum states, as well as the free-carrier plasma effect.

3.3 FREE-RUNNING QUANTUM DOT LASERS

3.3.1 Amplitude Modulation Response

High-speed, energy-effective, and low-cost optical communication networks primarily require semiconductor laser sources of broad modulation bandwidth. In order to theoretically discuss the amplitude modulation (AM) performance of Qdot lasers, we employ a semiclassical rate equation model [76]. The model will be analyzed in a semianalytical approach, which has the merit of giving an intuitive physical image. This numerical model of the Qdot laser holds under the assumption that the active region consists of only one Qdot ensemble; that is, the inhomogeneous broadening due to the dot size fluctuation is not considered. The electrons and holes are treated as electron–hole (e–h) pairs, meaning that the system is in excitonic energy states. Two discrete states in Qdots are taken into account: a twofold degenerate GS and a fourfold degenerate first ES. The Qdots are interconnected by the 2D RS. This simplified picture corresponds to the TRPL experimental observations in Figure 3.5 [75]. Carriers are supposed to be injected directly from the contacts into the RS, so the carrier dynamics in the 3D barrier are not taken into account in the model.

AQ3

AQ4

Figure 3.6 shows the schematic of the carrier dynamics in the conduction band. First, the externally injected carrier fills directly the RS reservoir; some of the carriers are then either captured into the ES within time τ_{ES}^{RS} or directly into the GS within time τ_{GS}^{RS}, and some of them recombine spontaneously with a spontaneous emission time τ_{RS}^{spon}. Once in the ES, carriers can relax into the GS within time τ_{GS}^{ES} or recombine spontaneously. On the other hand, carriers can also be thermally re-emitted from the ES to the RS with an escape time τ_{RS}^{ES}, which is governed by the Fermi distribution for the quasi-thermal equilibrium without external excitation [113]. A similar dynamic behavior is followed for the carrier population on the GS level with regard to the ES. Direct injection from the RS to the GS was introduced to reproduce the experimental results [76]. Stimulated emission occurs from the GS when the threshold is reached, and that from the ES is not taken into account in the model. Following Figure 3.6, the four coupled rate equations on carrier and photon densities are described as follows:

$$\frac{dN_{RS}}{dt} = \frac{I}{qV} + \frac{N_{ES}}{\tau_{RS}^{ES}} - \frac{N_{RS}}{\tau_{ES}^{RS}}(1-\rho_{ES}) - \frac{N_{RS}}{\tau_{GS}^{RS}}(1-\rho_{GS}) - \frac{N_{RS}}{\tau_{RS}^{spon}} + \frac{N_{GS}}{\tau_{RS}^{GS}} \tag{3.16}$$

$$\frac{dN_{ES}}{dt} = \frac{N_{RS}}{\tau_{ES}^{RS}}(1-\rho_{ES}) + \frac{N_{GS}}{\tau_{ES}^{GS}}(1-\rho_{ES}) - \frac{N_{ES}}{\tau_{RS}^{ES}} - \frac{N_{ES}}{\tau_{GS}^{ES}}(1-\rho_{GS}) - \frac{N_{ES}}{\tau_{ES}^{spon}} \tag{3.17}$$

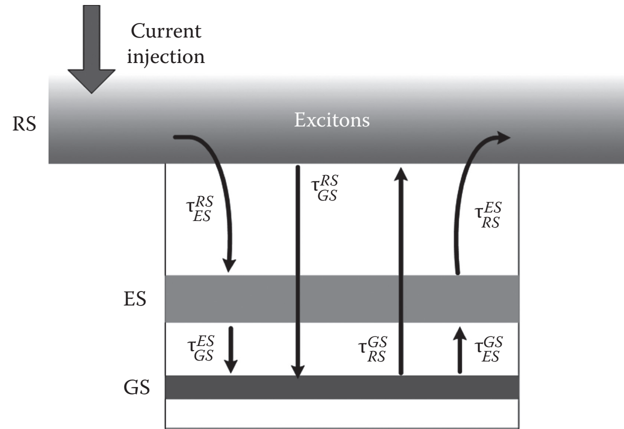

FIGURE 3.6 Sketch of carrier dynamics model including a direct relaxation channel.

$$\frac{dN_{GS}}{dt}=\frac{N_{RS}}{\tau_{GS}^{RS}}(1-\rho_{GS})+\frac{N_{ES}}{\tau_{GS}^{ES}}(1-\rho_{GS})-\frac{N_{GS}}{\tau_{ES}^{GS}}(1-\rho_{ES})-\frac{N_{GS}}{\tau_{GS}^{spon}}-\frac{N_{GS}}{\tau_{WL}^{GS}}-g_{GS}v_gS_{GS} \tag{3.18}$$

$$\frac{dS_{GS}}{dt}=\Gamma_p g_{GS}v_gS_{GS}-\frac{S_{GS}}{\tau_P}+\beta_{SP}\frac{N_{GS}}{\tau_{GS}^{spon}} \tag{3.19}$$

where
N_{RS}, N_{ES}, and N_{GS} are the carrier densities in the RS, ES, GS, respectively
S_{GS} is the photon density in the cavity with GS resonance energy
β_{SP} is the spontaneous emission factor
Γ_p is the optical confinement factor
AQ5 τ_p is the photon lifetime
v_g is the group velocity
V is the volume of the laser's active region

The GS gain is given by

$$g_{GS}=a_{GS}\frac{N_B}{H_B}\left(\frac{2N_{GS}}{2N_B/H_B}-1\right) \tag{3.20}$$

where
a_{GS} is the differential gain
N_B is the total Qdot surface density
H_B is the height of the dots.

In what follows, it is important to stress that the effects of gain compression are not taken into account. In Equations 3.16 through 3.18, $\rho_{GS,ES}$ are the carrier occupation probabilities in the GS and the ES, respectively:

$$\rho_{GS}=\frac{N_{GS}}{2N_B/H_B};\quad \rho_{ES}=\frac{N_{ES}}{4N_B/H_B} \tag{3.21}$$

Since the carrier escape from the GS to the RS has little effect on lasing properties [76], the N_{GS}/τ_{RS}^{GS} term in Equations 3.16 and 3.18 can be neglected.

The rate equations can be linearized through a small-signal analysis. Assuming a sinusoidal current modulation $dI = I_1 ej\omega t$ with modulation frequency ω, the corresponding carrier and photon variations are of the form

$$\begin{aligned} dN_{RS,ES,GS} &= N_{RS1,ES1,GS1}e^{j\omega t} \\ dS_{GS} &= S_{GS1}e^{j\omega t} \end{aligned} \tag{3.22}$$

Substituting the above formulas into the rate equations (Equations 3.16 through 3.18), we obtain the linearized differential rate equation in matrix form:

$$\begin{bmatrix} \gamma_{11}+j\omega & -\gamma_{12} & 0 & 0 \\ -\gamma_{21} & \gamma_{22}+j\omega & -\gamma_{23} & 0 \\ -\gamma_{31} & -\gamma_{32} & \gamma_{33}+j\omega & -\gamma_{34} \\ 0 & 0 & -\gamma_{43} & \gamma_{44}+j\omega \end{bmatrix} \begin{bmatrix} N_{RS1} \\ N_{ES1} \\ N_{GS1} \\ S_{GS1} \end{bmatrix} = \frac{I_1}{qV} \begin{bmatrix} 1 \\ 0 \\ 0 \\ 0 \end{bmatrix} \tag{3.23}$$

with the following elements:

$$\begin{aligned}
&\gamma_{11} = \frac{1-\rho_{ES}}{\tau_{ES}^{RS}} + \frac{1-\rho_{GS}}{\tau_{GS}^{RS}} + \frac{1}{\tau_{RS}^{spon}}; \quad \gamma_{12} = \frac{1}{\tau_{RS}^{ES}} + \frac{N_{RS}}{\tau_{ES}^{RS}} \frac{1}{4N_B/H_B} \\
&\gamma_{21} = \frac{1-\rho_{ES}}{\tau_{ES}^{RS}}; \quad \gamma_{22} = \frac{1-\rho_{GS}}{\tau_{GS}^{ES}} + \frac{1}{\tau_{RS}^{ES}} + \frac{N_{RS}}{\tau_{ES}^{RS}} \frac{1}{4N_B/H_B} + \frac{N_{GS}}{\tau_{ES}^{GS}} \frac{1}{4N_B/H_B} + \frac{1}{\tau_{ES}^{spon}} \\
&\gamma_{23} = \frac{1-\rho_{ES}}{\tau_{ES}^{GS}} + \frac{N_{ES}}{\tau_{GS}^{ES}} \frac{1}{2N_B/H_B}; \quad \gamma_{31} = \frac{1-\rho_{GS}}{\tau_{GS}^{RS}}; \quad \gamma_{32} = \frac{1-\rho_{GS}}{\tau_{GS}^{ES}} + \frac{N_{GS}}{\tau_{ES}^{GS}} \frac{1}{4N_B/H_B} \\
&\gamma_{33} = \frac{1-\rho_{ES}}{\tau_{ES}^{GS}} + \frac{N_{ES}}{\tau_{GS}^{ES}} \frac{1}{2N_B/H_B} + v_g a_{GS} S_{GS} + \frac{1}{\tau_{GS}^{spon}}; \quad \gamma_{34} = -v_g g_{GS} \\
&\gamma_{43} = \frac{\Gamma_p \beta_{SP}}{\tau_{GS}^{spon}} + \Gamma_p v_g a_{GS} S_{GS}; \quad \gamma_{44} = \frac{1}{\tau_p} - \Gamma_p v_g g_{GS}
\end{aligned} \tag{3.24}$$

Finally, the AM or intensity modulation response of the Qdot laser is calculated by

$$H_{Qdot}(\omega) = \frac{S_{GS1}}{I_1/(qV)} \tag{3.25}$$

This equation is also known as the *modulation transfer function*. Through proper approximation, the AM response is given by [114]

$$\begin{aligned} H_{Qdot}(\omega) &\approx H_1(\omega)H_0(\omega) \\ &= \left(\frac{\omega_R^2}{\omega_R^2 - \omega^2 + j\omega\Gamma} \right) \left(\frac{\omega_{R0}^2}{\omega_{R0}^2 - \omega^2 + j\omega\Gamma_0} \right) \end{aligned} \tag{3.26}$$

where the first part, $H_1(\omega)$, is dominated by the carrier–photon interaction processes. The resonance frequency ω_R and the damping factor Γ of the Qdot laser are, respectively, expressed as

$$\omega_R^2 = \frac{v_g a_{GS} S_{GS}}{\tau_p} + \frac{\Gamma_p \beta_{SP} N_{GS}}{\tau_{GS}^{spon} S_{GS}} \left[\left(\frac{H_B}{2N_B} \frac{N_{ES}}{\tau_{GS}^{ES}} + \frac{1-\rho_{ES}}{\tau_{ES}^{GS}} \right) + \frac{1-\beta_{SP}}{\tau_{GS}^{spon}} \right] + \frac{\beta_{SP}}{\tau_{GS}^{spon} \tau_p} \tag{3.27}$$

$$\Gamma = v_g a_{GS} S_{GS} + \left(\frac{H_B}{2N_B} \frac{N_{ES}}{\tau_{GS}^{ES}} + \frac{1-\rho_{ES}}{\tau_{ES}^{GS}} \right) + \frac{1}{\tau_{GS}^{spon}} + \frac{\Gamma_p \beta_{SP} N_{GS}}{\tau_{GS}^{spon} S_{GS}} \tag{3.28}$$

where the steady-state relationship $1/\tau_p - \Gamma_p v_g g_{GS} = \Gamma_p \beta_{SP} N_{GS}/(\tau_{GS}^{spon} S_{GS})$ has been used. In comparison with Qwell lasers [78], both expressions have an additional term $(H_B N_{ES}/(2N_B \tau_{GS}^{ES}) + (1-\rho_{ES})/\tau_{ES}^{GS})$, which describes the effective carrier scattering rate into and out of the GS. The second part, $H_0(\omega)$, is dominated by the carrier capture and relaxation processes, and the introduced two parameters ω_{R0} and Γ_0 are given by

$$\begin{aligned} \omega_{R0}^2 = & \left(\frac{1-\rho_{ES}}{\tau_{ES}^{RS}} + \frac{1}{\tau_{RS}^{spon}} \right) \left(\frac{1-\rho_{GS}}{\tau_{GS}^{ES}} + \frac{1}{\tau_{ES}^{spon}} + \frac{H_B}{4N_B} \frac{N_{RS}}{\tau_{ES}^{RS}} + \frac{H_B}{4N_B} \frac{N_{GS}}{\tau_{ES}^{GS}} \right) \\ & + \frac{1}{\tau_{RS}^{ES}} \frac{1}{\tau_{RS}^{spon}} - \frac{H_B}{4N_B} \frac{N_{RS}}{\tau_{ES}^{RS}} \frac{1-\rho_{ES}}{\tau_{ES}^{RS}} \end{aligned} \tag{3.29}$$

$$\Gamma_0 = \left(\frac{1-\rho_{ES}}{\tau_{ES}^{RS}} + \frac{1-\rho_{GS}}{\tau_{GS}^{RS}} + \frac{1}{\tau_{RS}^{spon}} \right) \left(\frac{1-\rho_{GS}}{\tau_{GS}^{ES}} + \frac{1}{\tau_{RS}^{ES}} + \frac{N_{RS}}{\tau_{ES}^{RS}} \frac{1}{4N_B/H_B} + \frac{N_{GS}}{\tau_{ES}^{GS}} \frac{1}{4N_B/H_B} + \frac{1}{\tau_{ES}^{spon}} \right) \tag{3.30}$$

Figure 3.7 presents an example of the calculated AM response of a Qdot laser. The solid curve $H_{Qdot}(\omega)$ shows that the response is strongly damped as usually observed in experiments [115–117], which can be attributed to the carrier relaxation and escape process of the GS as described in

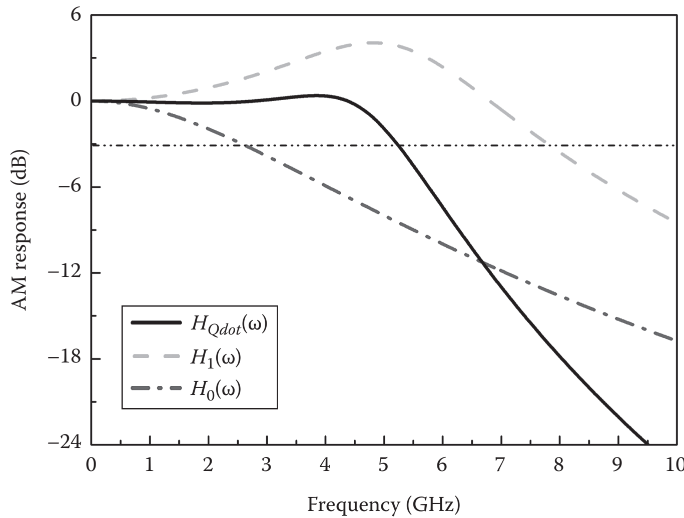

FIGURE 3.7 AM response $H_{Qdot}(\omega)$ (solid curve) of the Qdot laser. $H_1(\omega)$ (dash curve) describes mainly the contribution of carrier–photon interactions, and $H_0(\omega)$ (dash-dot curve) gives the contribution of carrier capture and relaxation processes. (From Wang, C. et al., *IEEE J. Quantum Electron.*, 48, 1144, 2012.)

Equation 3.28. On the other hand, $H_0(\omega)$ (dash-dot) exhibits a much smaller bandwidth than $H_1(\omega)$ (dash), which demonstrates that the finite carrier capture and relaxation times limit the modulation bandwidth of Qdot lasers.

3.3.2 Line-Width Enhancement Factor (α-Factor)

The line-width enhancement factor (α-factor) plays an important role in determining fundamental features of semiconductor lasers. Although the Qdot laser is predicted to have a delta-function-like discrete density of states, the measured α-factor values in experiments vary over a wide range from zero up to >10. The nonzero α-factor in Qdot lasers is partly attributed to the asymmetric gain spectrum because of the inhomogeneous broadening [118] and the carrier population in off-resonant states [119]. On the other hand, the free carrier plasma effect in the barrier and in the RS is reported to contribute almost half of the total refractive index change [100,101]. In this section, we describe an improved electric field model for Qdot lasers taking into account the contribution of off-resonant states (ES and RS) on the refractive index change, which allows a semianalytical study of the α-factor features in the Qdots. The model is capable of exploring the crucial physical mechanisms driving the Qdot laser's α-factor.

The conventional model describing the complex electric field of semiconductor lasers is given by

$$\frac{dE(t)}{dt} = \frac{1}{2}\left(\Gamma_P v_g g - \frac{1}{\tau_P}\right)E(t) + j\Delta\omega_N E(t) \tag{3.31}$$

where the first term on the right-hand side gives the gain and the photon loss of the laser cavity. The second term, $\Delta\omega_N$, describes the carrier-induced frequency shift of the laser field with respect to the frequency at the lasing threshold. $\Delta\omega_N$ is usually expressed by the α-factor α_H as

$$\Delta\omega_N = \frac{1}{2}\left(\Gamma_P v_g g - \frac{1}{\tau_P}\right)\alpha_H \tag{3.32}$$

This model is able to study the impacts of a nonzero α-factor on the modulation dynamics and nonlinear dynamics of Qdot lasers [120] but does not allow the study of α_H itself under different operating conditions. In order to investigate the α-factor, we need to obtain the expression of the gain and the refractive index separately. In the semiclassical theory, the semiconductor laser system can be fully described by the optical Bloch equations together with Maxell's equations [121]. The RS is treated as a discrete energy state of degeneracy $D_{RS} = k_B T m^* A_{RS}/(\pi\hbar^2)$, with m^* the reduced carrier mass and A_{RS} the RS surface area (see Section 3.1) [122]. The active region consists of only one Qdot ensemble. In addition, the electrons and holes are treated as neutral pairs (excitons). Two discrete states—the ground state (GS) and the first excited state (ES)—are considered in the dots. With these assumptions, the slowly varying electric field $E(t)$ is given by [123]

$$\frac{d}{dt}E(t) = \frac{j\omega_{LS}^0\Gamma_P}{2\varepsilon_{bg}\varepsilon_0}\frac{1}{A_{RS}H_B}\sum_{X=GS,\,ES,\,RS}\left(\mu_X^* P_X\right) - \frac{1}{2\tau_P}E(t) \tag{3.33}$$

where

ω_{LS}^0 is the lasing frequency in the cold cavity

ε_{bg} and ε_0 are the background and vacuum permittivity, respectively

AQ6 Γ_P is the optical confinement factor

H_B is the height (equal to the dot's height)

The sum over X (X = GS, ES, RS) includes all possible optical transitions, with μ_X being the corresponding dipole transition matrix element and P_X the microscopic polarization. τ_P is the photon lifetime in the laser cavity. Assuming a sufficiently short dephasing time T_D and adiabatically eliminating the interband polarization yields the quasi-static relation

$$P_X(t) = -j\frac{\mu_X T_D}{2\hbar}(2\rho_X - 1)\frac{1 + j(\omega_X - \omega_{LS}^0)T_D}{1 + (\omega_X - \omega_{LS}^0)^2 T_D^2}E(t) \tag{3.34}$$

where

ρ_X denotes the carrier occupation probability

$\hbar\omega_X$ gives the transition energy of each state

Inserting Equation 3.34 into Equation 3.33, we obtain the complex gain

$$\tilde{G}(\omega_{LS}^0, t) = \left(2\mu_{GS}^*\frac{j\omega_{LS}^0\Gamma_P}{2\varepsilon_0\varepsilon_{bg}}\frac{2N_B}{H_B}\frac{P_{GS}(t)}{E(t)}\right) + \left(4\mu_{ES}^*\frac{j\omega_{LS}^0\Gamma_P}{2\varepsilon_0\varepsilon_{bg}}\frac{2N_B}{H_B}\frac{P_{ES}(t)}{E(t)}\right) + \left(\frac{j\omega_{LS}^0\Gamma_P}{2\varepsilon_0\varepsilon_{bg}}\frac{2}{A_{RS}H_B}D_{RS}\mu_{RS}^*\frac{P_{RS}(t)}{E(t)}\right) \tag{3.35}$$

The optical susceptibility can be derived from this complex gain expression through the relationship $\chi(\omega_{LS}^0, t) = 2\varepsilon_{bg}\tilde{G}(\omega_{LS}^0, t)/(j\omega\Gamma_P)$. The real part of Equation 3.35 is related to the laser gain, while the imaginary part gives the instantaneous frequency shift of the electric field. The three terms on the right-hand side give contributions of the GS, ES, and RS, respectively. Introducing the differential gain (a_X), we have

$$a_{GS} = \frac{2\mu_{GS}\mu_{GS}^*\omega_{GS}T_D}{\hbar v_g\varepsilon_0\varepsilon_{bg}}$$
$$a_{ES} = \frac{4\mu_{ES}\mu_{ES}^*\omega_{ES}T_D}{\hbar v_g\varepsilon_0\varepsilon_{bg}} \tag{3.36}$$
$$a_{RS} = \frac{\mu_{RS}\mu_{RS}^*\omega_{RS}T_D}{\hbar v_g\varepsilon_0\varepsilon_{bg}}$$

with v_g being the group velocity of the light. The material gain of each state is then given by

$$g_{GS} = \frac{a_{GS}}{1 + \xi S_{GS}}\frac{N_B}{H_B}\left(\frac{2N_{GS}}{2N_B/H_B} - 1\right)$$
$$g_{ES} = a_{ES}\frac{N_B}{H_B}\left(\frac{2N_{ES}}{4N_B/H_B} - 1\right) \tag{3.37}$$
$$g_{RS} = a_{RS}\frac{D_{RS}}{A_{RS}H_B}\left(\frac{2N_{RS}}{D_{RS}/(A_{RS}H_B)} - 1\right)$$

where

N_X is the carrier density in each state

S_{GS} is the photon density in the GS

ξ denotes the gain compression factor

Because the real part of the complex gain approaches zero very quickly when off resonance, the field gain originates mainly from the resonant state. Considering the lasing emission in resonance with the GS transition $\omega_{LS}^0 = \omega_{GS}$, we obtain

$$\mathrm{Re}[\tilde{G}(\omega_{GS})] \approx \Gamma_P v_g g_{GS} \tag{3.38}$$

In contrast, the imaginary part of the complex gain decays slowly for off-resonant frequencies. Thus, the off-resonant states can significantly influence the refractive index change, even though their gain contribution to the GS lasing is almost nil. Carrier populations in the off-resonant ES and RS induced frequency shifts of the laser field respectively are

$$\Delta\omega_N^{ES} = \frac{1}{2}\Gamma_P v_g g_{ES} F_{ES}^{GS} \tag{3.39}$$

$$\Delta\omega_N^{RS} = \frac{1}{2}\Gamma_P v_g g_{RS} F_{RS}^{GS} \tag{3.40}$$

with coefficients

$$F_{ES,RS}^{GS} = \frac{\omega_{GS}}{\omega_{ES,RS}} \frac{(\omega_{ES,RS} - \omega_{GS})T_D}{1 + (\omega_{ES,RS} - \omega_{GS})^2 T_D^2} \tag{3.41}$$

From Equation 3.35, it is seen that the resonant GS has no contribution to the refractive index change, which is the case when the laser is operated at the gain peak with a symmetric gain distribution. Nevertheless, as mentioned in the introduction, due to the asymmetric Qdot size dispersion, the resonant state induces a finite α-factor α_H^{GS}, and the corresponding frequency shift with respect to the cold cavity can be expressed by

$$\Delta\omega_N^{GS} = \frac{1}{2}\Gamma_P v_g g_{GS} \alpha_H^{GS} \tag{3.42}$$

Employing Equations 3.37 through 3.42, the electric field (Equation 3.33) is re-expressed as

$$\frac{dE(t)}{dt} = \frac{1}{2}\left(\Gamma_P v_g g_{GS} - \frac{1}{\tau_P}\right)E(t) + j\left(\Delta\omega_N^{GS} + \Delta\omega_N^{ES} + \Delta\omega_N^{RS}\right)E(t) \tag{3.43}$$

With carrier injection, the lasing frequency becomes $\omega_{LS} = \omega_{th}^{LS} + \Delta\omega_N^{LS}$, where $\Delta\omega_N^{LS} = \Delta\omega_N^{GS} + \Delta\omega_N^{ES} + \Delta\omega_N^{RS}$ gives the total frequency shift of the electric field from its threshold value (ω_{th}^{LS}). Through the $E(t) = \sqrt{S(t)V/\Gamma_P}\, e^{j\phi(t)}$ relationship, the photon density $S(t)$ and the phase $\phi(t)$ can be separately described. Combining with the equations describing the carrier dynamics in Qdot lasers, the laser system is finally given by

$$\frac{dN_{RS}}{dt} = \frac{I}{qV} + \frac{N_{ES}}{\tau_{RS}^{ES}} - \frac{N_{RS}}{\tau_{ES}^{RS}}(1 - \rho_{ES}) - \frac{N_{RS}}{\tau_{RS}^{spon}} \tag{3.44}$$

$$\frac{dN_{ES}}{dt} = \left(\frac{N_{RS}}{\tau_{ES}^{RS}} + \frac{N_{GS}}{\tau_{ES}^{GS}}\right)(1 - \rho_{ES}) - \frac{N_{ES}}{\tau_{GS}^{ES}}(1 - \rho_{GS}) - \frac{N_{ES}}{\tau_{RS}^{ES}} - \frac{N_{ES}}{\tau_{ES}^{spon}} \tag{3.45}$$

$$\frac{dN_{GS}}{dt} = \frac{N_{ES}}{\tau_{GS}^{ES}}(1-\rho_{GS}) - \frac{N_{GS}}{\tau_{ES}^{GS}}(1-\rho_{ES}) - v_g g_{GS} S_{GS} - \frac{N_{GS}}{\tau_{GS}^{spon}} \tag{3.46}$$

$$\frac{dS_{GS}}{dt} = \left(\Gamma_p v_g g_{GS} - \frac{1}{\tau_P}\right) S_{GS} + \beta_{SP}\frac{N_{GS}}{\tau_{GS}^{spon}} \tag{3.47}$$

$$\frac{d\phi}{dt} = \Delta\omega_N^{GS} + \Delta\omega_N^{ES} + \Delta\omega_N^{RS} \tag{3.48}$$

where

τ_{GS}^{spon} is the spontaneous emission time
β_{SP} is the spontaneous emission factor

Carriers in the RS are scattered into the dots through phonon-assisted and Auger-assisted processes [82,83]. The latter makes the scattering rates nonlinearly depend on the carrier density in the RS. However, for the sake of simplicity, the carrier capture time τ_{ES}^{RS} and the relaxation time τ_{GS}^{ES} are both treated as constants in this work. On the other hand, the carrier escape times ($\tau_{RS}^{ES}, \tau_{ES}^{GS}$) are governed by the Fermi distribution for a quasi-thermal equilibrium system [124]. For semiconductor lasers operating under small-signal modulation with frequency ω, the bias current change δI induces variations of the carriers δN_X, the photon δS_{GS}, and the phase $\delta\phi$. In order to perform the analyses, the differential rate equations are derived as follows:

$$\begin{bmatrix} \gamma_{11}+j\omega & -\gamma_{12} & 0 & 0 & 0 \\ -\gamma_{21} & \gamma_{22}+j\omega & -\gamma_{23} & 0 & 0 \\ 0 & -\gamma_{32} & \gamma_{33}+j\omega & -\gamma_{34} & 0 \\ 0 & 0 & -\gamma_{43} & \gamma_{44}+j\omega & 0 \\ -\gamma_{51} & -\gamma_{52} & -\gamma_{53} & -\gamma_{54} & j\omega \end{bmatrix} \begin{bmatrix} \delta N_{RS} \\ \delta N_{ES} \\ \delta N_{GS} \\ \delta S_{GS} \\ \delta\phi \end{bmatrix} = \frac{\delta I}{qV}\begin{bmatrix} 1 \\ 0 \\ 0 \\ 0 \\ 0 \end{bmatrix} \tag{3.49}$$

where

$$\gamma_{11} = \frac{1-\rho_{ES}}{\tau_{ES}^{RS}} + \frac{1}{\tau_{RS}^{spon}}; \quad \gamma_{12} = \frac{1}{\tau_{RS}^{ES}} + \frac{1}{4N_B}\frac{N_{RS}}{\tau_{ES}^{RS}}; \quad \gamma_{21} = \frac{1-\rho_{ES}}{\tau_{ES}^{RS}};$$

$$\gamma_{22} = \frac{1-\rho_{GS}}{\tau_{GS}^{ES}} + \frac{1}{\tau_{RS}^{ES}} + \frac{1}{\tau_{ES}^{spon}} + \frac{1}{4N_B}\frac{N_{RS}}{\tau_{ES}^{RS}} + \frac{1}{4N_B}\frac{N_{GS}}{\tau_{ES}^{GS}}$$

$$\gamma_{23} = \frac{1-\rho_{ES}}{\tau_{ES}^{GS}} + \frac{1}{2N_B}\frac{N_{ES}}{\tau_{GS}^{ES}}; \quad \gamma_{32} = \frac{1-\rho_{GS}}{\tau_{GS}^{ES}} + \frac{1}{4N_B}\frac{N_{GS}}{\tau_{ES}^{GS}}; \quad \gamma_{33} = \frac{1-\rho_{ES}}{\tau_{ES}^{GS}} + \frac{1}{\tau_{GS}^{spon}} + \frac{1}{2N_B}\frac{N_{ES}}{\tau_{GS}^{ES}} + v_g a S_{GS}$$

$$\gamma_{34} = -v_g g_{GS} + v_g a_P S_{GS}; \quad \gamma_{43} = \Gamma_p v_g a S_{GS} + \frac{\Gamma_p \beta_{SP}}{\tau_{GS}^{spon}};$$

$$\gamma_{44} = -\Gamma_p v_g g_{GS} + \frac{1}{\tau_p} + \Gamma_p v_g a_P S_{GS}; \quad \gamma_{51} = \Gamma_p v_g a_{RS} F_{RS}$$

$$\gamma_{52} = \frac{1}{4}\Gamma_p v_g a_{ES} F_{ES}; \quad \gamma_{53} = \frac{1}{2}\Gamma_p v_g a \alpha_H^{GS}; \quad \gamma_{54} = -\frac{1}{2}\Gamma_p v_g a_P \alpha_H^{GS} \tag{3.50}$$

with

$$a = \frac{\partial g_{GS}}{\partial N_{GS}} = \frac{a_{GS}}{1+\xi S_{GS}}; \quad a_P = -\frac{\partial g_{GS}}{\partial S_{GS}} = \frac{\xi}{1+\xi S_{GS}} g_{GS} \tag{3.51}$$

Based on the above differential rate equations, the α-factor of the Qdot laser is derived as

$$\alpha_{H,QD}^{GS}(\omega) = \frac{2}{\Gamma_P v_g} \frac{\delta\left[\Delta\omega_N^{LS}(N)\right]}{\delta g_{GS}(N)} \equiv \alpha_H^{GS} + \frac{1}{2} F_{ES} \frac{a_{ES}\delta N_{ES}}{a\delta N_{GS}} + 2F_{RS} \frac{a_{RS}\delta N_{RS}}{a\delta N_{GS}} \tag{3.52}$$

Following the definition in Equation 3.13, it is noted that only the carrier contribution (δN) is included in the above equation, while the photon contribution (δS) is excluded. In the following, it will be shown that the α-factor of Qdot lasers presents peculiar characteristics under direct modulation.

Over the last decades, various techniques have been proposed for the measurement of the α-factor. In this work, we employ the well-known "FM/AM" technique for the above-threshold analysis and the widely used "Hakki-Paoli" method for the below-threshold analysis [102]. The FM/AM technique relies on the direct current modulation of the laser, which generates both the optical frequency (FM) and amplitude (AM) modulations [125]. With respect to the linearized rate equations, the ratio of the FM/AM index is derived as

$$\begin{aligned} 2\frac{\beta(\omega)}{m(\omega)} &= 2\frac{\delta\omega_{LS}/\omega}{\delta S_{GS}/S_{GS}} \\ &\equiv \frac{j\omega + (1/\tau_P - \Gamma_P v_g g_{GS} + \Gamma_p v_g a_P S_{GS})}{j\omega} \times \left[\alpha_H^{GS}\left(1 - \frac{a_P \delta S_{GS}}{a\delta N_{GS}}\right) + \frac{1}{2} F_{ES} \frac{a_{ES}\delta N_{ES}}{a\delta N_{GS}} + 2F_{RS} \frac{a_{RS}\delta N_{RS}}{a\delta N_{GS}}\right] \end{aligned} \tag{3.53}$$

where the relation $\delta\omega_{LS} = j\omega\delta\phi$ is used in the above derivation. In this approach, the laser's α-factor is usually extracted through the formula $\alpha_{H,QD}^{FM/AM} = \min\{2\beta(\omega)/m(\omega)\}$. This is indeed true for Qwell or bulk lasers; however, we show that the α-factor of Qdot lasers is dependent on the modulation frequency but we still take the minimum value to characterize the Qdot laser as reported in [119].

For semiconductor lasers operating below threshold, the Hakki-Paoli method relies on the direct measurement of the optical spectra of amplified spontaneous emission (ASE) in the laser cavity. Tuning the pump current slightly step by step (ΔI), the gain change can be extracted by the Hakki-Paoli method, and the wavelength variation can be directly recorded using an optical spectrum analyzer. Correspondingly, the below-threshold α-factor is calculated as

$$\alpha_{H,QD}^{ASE} = \alpha_H^{GS} + \frac{1}{2} F_{ES}^{GS} \frac{a_{ES}}{a_{GS}} \frac{\Delta N_{ES}}{\Delta N_{GS}} + 2F_{RS}^{GS} \frac{a_{RS}}{a_{GS}} \frac{\Delta N_{RS}}{\Delta N_{GS}} \tag{3.54}$$

The laser parameters used in the simulation are listed in Table 3.2 [57,75,126]. It is noted that the carrier occupation in the GS has a small contribution to the α-factor (<1) [127]; hence we assume the value $\alpha_H^{GS} = 0.5$ in the simulation. Figure 3.8a depicts the carrier density variations in the three states under small-signal modulation. For low frequencies (smaller than 0.1 GHz), all the carrier density variations remain almost constant, but the variations of the ES (δN_{ES}) and RS (δN_{RS}) populations are 15 dB larger than that of the GS (δN_{GS}) one. The small variation of the GS carrier population is associated with the gain-clamping above the threshold. Both δN_{GS} and δN_{ES} exhibit resonances at ~7 GHz. Beyond the resonance frequency, δN_{GS} decays faster than δN_{ES} and δN_{RS}. These features significantly impact the behavior of the α-factor, as described in Equation 3.52.

TABLE 3.2
Qdot Material and Laser Parameters for the Study of the α-Factor

Symbol	Description	Value	Symbol	Description	Value
L	Active region length	5×10^{-2} cm	τ_{ES}^{RS}	Capture time from RS to ES	6.3 ps
W	Active region width	4×10^{-4} cm	τ_{GS}^{ES}	Relaxation time from ES to GS	2.9 ps
$R_1 = R_2$	Mirror reflectivity	0.32	a_{GS}	GS differential gain	5×10^{-15} cm^2
n_r	Refractive index	3.5	a_{ES}	ES differential gain	10×10^{-15} cm^2
α_i	Internal modal loss	6 cm^{-1}	a_{RS}	RS differential gain	2.5×10^{-15} cm^2
N_B	Dot density	10×10^{10} cm^{-2}	ξ	Gain compression factor	2×10^{-16} cm^3
H_B	Dot height	5×10^{-7} cm	α_H^{GS}	GS induced α-factor	0.5
E_{RS}	RS transition energy	0.97 eV	T_D	Dephasing time	0.1 ps
E_{ES}	ES transition energy	0.87 eV	Γ_p	Optical confinement factor	0.06
E_{GS}	GS transition energy	0.82 eV	β_{SP}	Spontaneous emission factor	1×10^{-4}

Figure 3.8b compares the difference between the α-factor $\left|\alpha_{H,QD}^{GS}(\omega)\right|$ and the ratio $\left|2\beta(\omega)/m(\omega)\right|$ as a function of the modulation frequency. At low frequencies (<0.1 GHz), there is a large discrepancy between the two parameters. As expected, $|2\beta(\omega)/m(\omega)|$ exhibits large values due to the gain compression and the large carrier variations in the ES and in the RS. Nevertheless, $\left|\alpha_{H,QD}^{GS}(\omega)\right|$ remains constant. On increasing the modulation frequency beyond several gigahertz, the two values of both parameters decrease down to a plateau, which gives the conventional α-factor, indicated by the horizontal line. As can be seen, $\alpha_{H,QD}^{FM/AM}$ is almost the same as $\left|\alpha_{H,QD}^{GS}\right|$, which indicates that the FM/AM method is a reliable technique for the measurement of Qdot laser's α-factor. Further increase of the modulation frequency raises again both the values, as observed experimentally in a Qdot laser (inset of Figure 3.8b) [129]. It is emphasized that such a situation is not encountered in Qwell lasers [125]. This behavior is attributed to the different decay rates (versus modulation frequency) of carrier variations in each state, as shown in Figure 3.8a. In addition, Figure 3.8b shows that the ES (dash-dot curves) contributes more to the α-factor $\left|\alpha_{H,QD}^{GS}\right|$ than the RS due to its smaller energy separation with the resonant GS.

Based on the ASE and the FM/AM methods, Figure 3.9 illustrates the α-factor as a function of the normalized pump current I/I_{th}. Below threshold, carrier populations in both the resonant and off-resonant states increase with the pump current. In consequence, the α-factor increases nonlinearly. Above threshold, the carrier population in the GS is clamped, while the off-resonant state populations keep increasing. Thus, the α-factor varies almost linearly above threshold as usually measured in experiments [57,71]. At threshold, the α-factor extracted from the ASE method is similar to that using the FM/AM technique. In addition, the α-factor is larger than the sole GS-induced value of $\alpha_H^{GS} = 0.5$ both below and above threshold, which means the off-resonant ES and RS contribute to the increase of the α-factor in the Qdot laser. This is explained by the fact that the coefficients F_{ES}^{GS} and F_{RS}^{GS} are both positive since the ES and RS have higher energies than the GS (see Equation 3.41).

3.3.3 Impacts of Carrier Capture and Relaxation Processes

As discussed previously, the Qdot laser involves a carrier capture process from the 2D RS to the localized ES and a carrier relaxation process from the ES to the GS inside the dots. This section discusses the influences of these processes on the laser's modulation dynamics.

In order to study the impacts of the carrier capture process, the carrier relaxation time τ_{GS}^{ES} is fixed at 2.9 ps, while the carrier capture time τ_{ES}^{RS} is varied from 0.1 up to 50 ps. Figure 3.10a shows the variation of the AM response for different capture times. Slow capture reduces the 3 dB

K13633_C003.indd 116 4/4/2016 4:18:07 PM

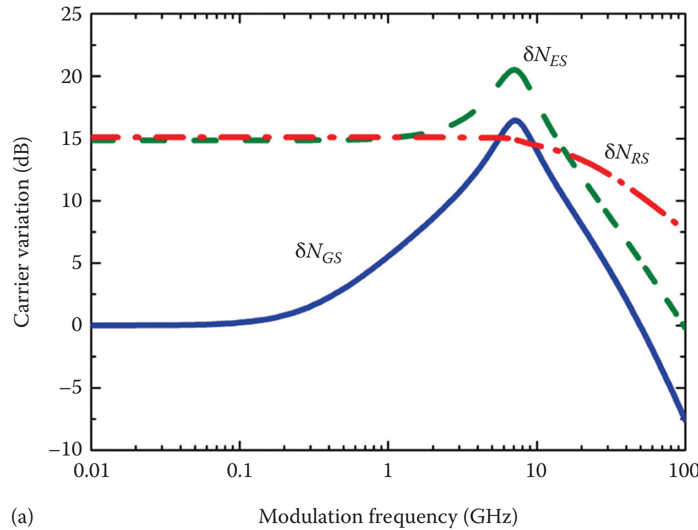

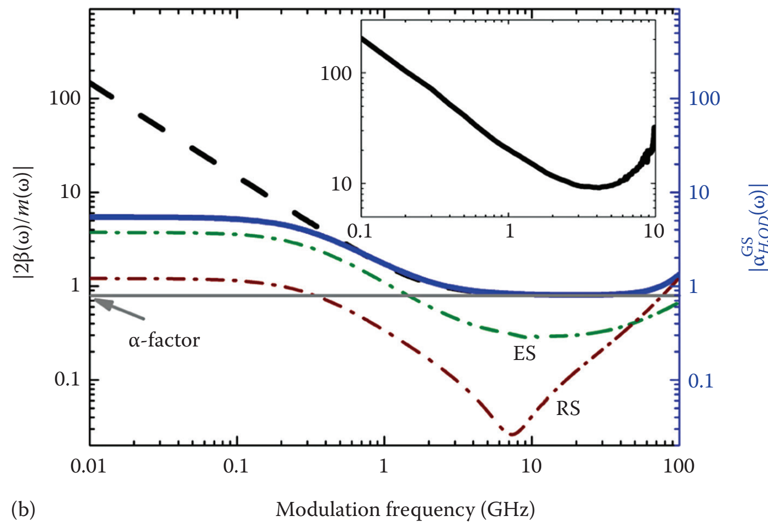

FIGURE 3.8 (a) Small-signal carrier density variations in the GS (solid line), ES (dashed line), and RS (dash-dot line) versus the modulation frequency. The bias current is $I = 1.2 \times I_{th}$, with the threshold current $I_{th} = 49$ mA. The carrier variation is normalized to the value δN_{GS} of 0.01 GHz. (b) Modulation-frequency dependence of the FM/AM ratio (dash) and of the α-factor (thick solid). The minimum level indicated by the horizontal line gives the laser's conventional α-factor. The thin dash-dotted curve represents the sole contribution of the ES or the RS to the α-factor, respectively. The inset shows an experimental curve of the FM/AM ratio for a Qdot laser. (From Wang, C. et al., *Appl. Phys. Lett.*, 105, 221114, 2014.)

modulation bandwidth from 11 GHz down to 7 GHz. Besides, the resonance peak is also slightly reduced. Interestingly, for capture times larger than 30 ps, a parasitic-like roll-off (dip) appears in the response, which is similar to the effect of the slow carrier transport process from the 3D barrier to the 2D RS [78]. In the same approach, by fixing the capture time at 6.3 ps, Figure 3.10b shows the impact of carrier relaxation time on the AM response. The modulation bandwidth is significantly reduced by the slow relaxation process from 10.8 GHz for $\tau_{GS}^{ES} = 0.1$ ps to 1.6 GHz for $\tau_{GS}^{ES} = 50$ ps. In addition, the response is strongly damped for large relaxation times. It is noted that the evolution of the AM response shape is quite different from that for the capture process in Figure 3.10a.

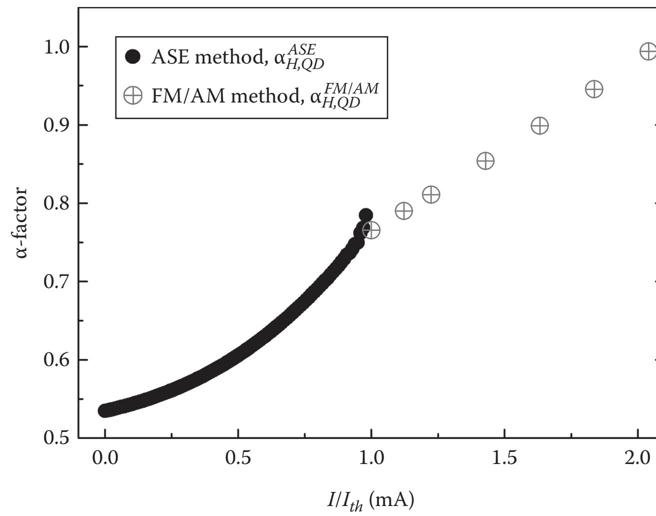

FIGURE 3.9 α-Factor as a function of the normalized bias current I/I_{th}. (From Wang, C. et al., *Appl. Phys. Lett.*, 105, 221114, 2014.)

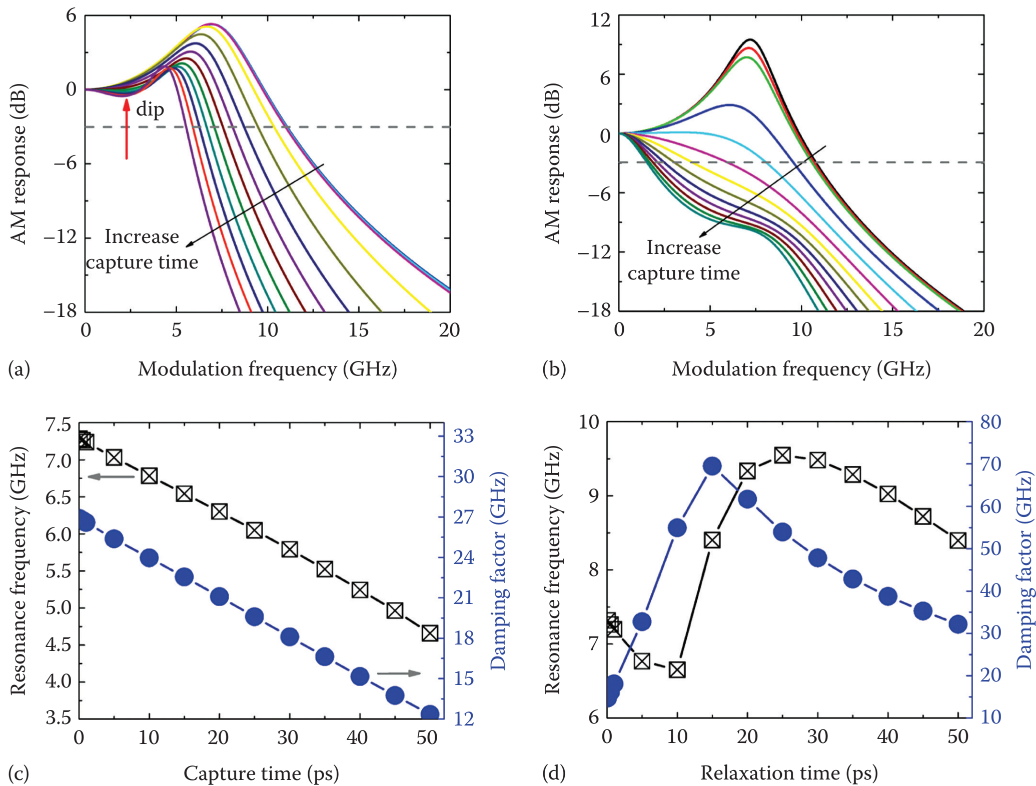

FIGURE 3.10 Influence of carrier scattering times on the AM response, resonance frequency, and damping factor. (a) and (c) are for the variation of capture time with fixed relaxation time at 2.9 ps. (b) and (d) are for the variation of relaxation time with fixed capture time at 6.3 ps.

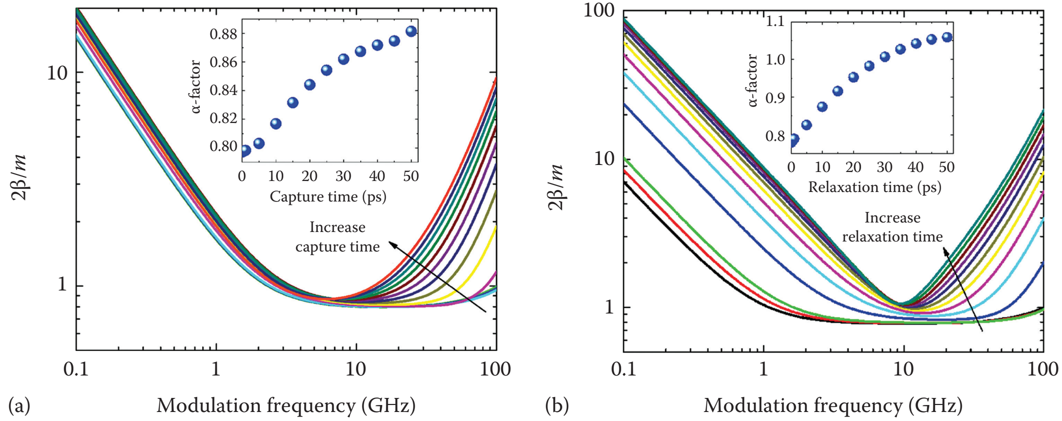

FIGURE 3.11 Influence of (a) the carrier capture time and (b) relaxation time on the ratio of FM/AM index. Insets show the α-factor variation extracted from the minimum of the FM/AM index ratio.

For relaxation times $\tau_{GS}^{ES} > 25$ ps, the response shows a clear resonance at ~8 GHz. From the eigenvalue analysis of the Qdot laser system [130], the resonance frequency f_R and the damping factor Γ are extracted for various carrier scattering times. It is shown that both f_R and Γ decrease linearly with increase in carrier capture time (Figure 3.10c). In contrast, for the carrier relaxation process (Figure 3.10d) the behavior is much more complex. The resonance frequency first decreases for $\tau_{GS}^{ES} < 10$ ps, while the damping factor increases with the relaxation time. At $\tau_{GS}^{ES} = 10$ ps, the AM response is rather flat. However, for $\tau_{GS}^{ES} > 10$ ps the resonance again increases until $\tau_{GS}^{ES} = 25$ ps, while the damping factor reaches the maximum at $\tau_{GS}^{ES} = 15$ ps. Beyond the peak values, both the resonance and damping decrease as a function of the relaxation time. Lastly, we note that the damping factors of the Qdot laser in both Figure 3.10c and d are much larger than those of Qwell lasers, which is attributed to the carrier occupation in the off-resonant states as well as the carrier scattering processes [131].

Figure 3.11a illustrates that the FM/AM index ratio $2\beta/m$ exhibits a significant re-increase beyond 10 GHz for a slow carrier capture process (large capture time). With respect to Equation 3.52, this can be attributed to the larger carrier variation in the RS, δN_{RS}, under high-frequency modulation since the number of available carriers in the RS is larger. The inset of Figure 3.11a indicates that increasing the carrier capture time enhances the α-factor by 11% from 0.80 for $\tau_{ES}^{RS} = 0.10$ ps to 0.88 for $\tau_{ES}^{RS} = 50$ ps. Figure 3.11b depicts that a slow carrier relaxation process induces a steep re-increase of $2\beta/m$ for modulation frequencies larger than 10 GHz. This is due to the increased carrier populations and variations in the ES and RS. The inset of Figure 3.11b shows the α-factor extracted from the minimum value of $2\beta/m$, which increases by about 36% from 0.78 for $\tau_{GS}^{ES} = 0.1$ ps to 1.06 for $\tau_{GS}^{ES} = 50$ ps.

3.4 CONCLUSION

In this chapter, we discussed the electronic and optical features of InP-based nanostructure semiconductor lasers. In contrast to conventional Qwell lasers, in Qdot and Qdash lasers the existence of a carrier reservoir, discrete excited states, and the consequent carrier scattering processes bring unique characteristics to the dynamic modulation response and the line-width enhancement factor. Regarding the dynamical performance, it can be well improved by the excited-state lasing instead of ground-state lasing [132]. On the other hand, nonlinear photonic techniques such as optical injection [133,134], optical feedback [135], and optoelectronic feedback [136] can be employed for further enhancement of the dynamical performance of nanostructure lasers.

ACKNOWLEDGMENTS

This work was supported in part by the Partenariat Hubert Curien under Grant No. 30794RC (Campus France/DAAD) and by the European Office for Aerospace Research (EOARD) under grant FA9550-15-1-0104.

REFERENCES

1. E. Murphy, Enabling optical communication, *Nat. Photon.* 4, 287 (2010).
2. H. Kroemer, Theory of a wide-gap emitter for transistors, *Proc. IRE* 45, 1535 (1957).
3. Z. I. Alferov and R. F. Kazarinov, Semiconductor laser with electric pumping, Inventor's Certificate 181737 in Russian, Application 950840, priority as of March 30, 1963.
4. R. Dingle and C. H. Henry, Quantum effects in heterostructure lasers, U.S. Patent No. 3,982,207, filed on March 7, 1975, issued September 21, 1976.
5. J. P. van der Ziel, R. Dingle, R. C. Miller, W. Wiegmann, and W. A. Nordland, Laser oscillations from quantum states in very thin GaAs-$Al_{0.2}Ga_{0.8}As$ multilayer structures, *Appl. Phys. Lett.* 26, 463 (1975).
6. Y. Arakawa and H. Sakaki, Multidimensional quantum well laser and temperature dependence of its threshold current, *Appl. Phys. Lett.* 40, 939 (1982).
7. M. Asada, Y. Miyamoto, and Y. Suematsu, Gain and the threshold of three-dimensional quantum-box lasers, *IEEE J. Quantum Electron.* 22, 1915 (1986).
8. D. Bimberg, M. Grundmann, and N. N. Ledentsov, *Quantum Dot Heterostructures*, New York: Wiley, 1998.
9. Y. Arakawa, Progress in growth and physics of nitride-based quantum dots, *Phys. Status Solidi* (*a*) 188, 37 (2001).
10. N. Kirstaedter, N. N. Ledentsov, M. Grundmann, D. Bimberg, V. M. Ustinov, S. S. Ruvimov, M. V. Maximov, P. S. Kop'ev, and Zh. I. Alferov, Low threshold, large T_0 injection laser emission from (InGa)As quantum dots, *Electron. Lett.* 30, 1416 (1994).
11. D. Bimberg et al., InAs-GaAs quantum pyramid lasers: In situ growth, radiative lifetimes and polarization properties, *Jpn. J. Appl. Phys.* 35, 1311 (1996).
12. N. N. Ledentsov et al., Direct formation of vertically coupled quantum dots in Stranski–Krastanow growth, *Phys. Rev. B* 54, 8743 (1996).
13. M. T. Crowley, N. A. Naderi, H. Su, F. Grillot, and L. F. Lester, GaAs based quantum dot lasers, in *Semiconductors and Semimetals: Advances in Semiconductor Lasers*, 2012. AQ7
14. H. Y. Liu, K. M. Groom, D. T. D. Childs, D. J. Robbins, T. J. Badcock, M. Hopkinson, D. J. Mowbray, and M. S. Skolnick, 1.3 μm InAs/GaAs multilayer quantum-dot laser with extremely low room temperature threshold current density, *Electron. Lett.* 40, 1412 (2004).
15. M. V. Maksimov et al., High-power 1.5 μm InAs-InGaAs quantum dot lasers on GaAs substrates, *Semiconductors* 38, 732 (2004).
16. A. Zhukov, M. Maksimov, and A. Kovsh, Device characteristics of long-wavelength lasers based on self-organized quantum dots, *Semiconductors* 46, 1225 (2012).
17. P. B. Joyce, T. J. Krzyzewski, P. H. Steans, G. R. Bell, J. H. Neave, and T. S. Jones, Variations in critical coverage for InAs/GaAs quantum dot formation in bilayer structures, *J. Cryst. Growth* 244, 39 (2002).
18. F. Y. Chang, C. C. Wu, and H. H. Lin, Effect of InGaAs capping layer on the properties of InAs/InGaAs quantum dots and lasers, *Appl. Phys. Lett.* 82, 4477 (2003).
19. J. Oshinowo, M. Nishioka, S. Ishida, and Y. Arakawa, Highly uniform InGaAs/GaAs quantum dots (15 nm) by metal organic chemical vapor deposition, *Appl. Phys. Lett.* 65, 1421 (1994).
20. P. J. Poole, K. Kaminska, P. Barrios, Z. Lu, and J. Liu, Growth of InAs/InP-based quantum dots for 1.55 μm laser applications, *J. Cryst. Growth* 311, 1482 (2009).
21. N. Bertru et al., QD laser on InP substrate for 1.55 μm emission and beyond, *Proc. SPIE* 7608, 76081B (2010).
22. M. Gong, K. Duan, C. F. Li, R. Magri, A. Narvaez, and L. He, Electronic structure of self-assembled InAs/InP quantum dots: Comparison with self-assembled InAs/GaAs quantum dots, *Phys. Rev. B* 77, 045326 (2008).
23. R. H. Wang, A. Stintz, P. M. Varangis, T. C. Newell, H. Li, K. J. Malloy, and L. F. Lester, Room-temperature operation of InAs quantum-dash lasers on InP(001), *IEEE Photon. Technol. Lett.* 13, 767 (2001).

24. P. Miska, J. Even, C. Platz, B. Salem, and T. Benyattou, Experimental and theoretical investigation of carrier confinement in InAs quantum dashes grown on InP(001), *J. Appl. Phys.* 95, 1074 (2004).

AQ8

25. M. Z. M. Khan, T. K. Ng, and B. S. Ooi, Self-assembled InAs/InP quantum dots and quantum dashes: Material structures and devices, *Prog. Quantum Electron.* (2014).
26. J. P. Reithmaier, G. Eisenstein, and A. Forchel, InAs/InP quantum-dash lasers and amplifiers, *Proc. IEEE* 95, 1779 (2007).

AQ9

27. D. Zhou, R. Piron, F. Grillot, O. Dehaese, E. Homeyer, M. Dontabactouny, T. Batte, K. Tavernier, J. Even, and S. Loualiche, Study of the characteristics of 1.55 μm quantum dash/dot semiconductor lasers on InP substrate, *Appl. Phys. Lett.* 93, 161104 (2008).
28. D. Zhou, R. Piron, M. Dontabactouny, O. Dehaese, F. Grillot, and T. Batte, Low threshold current density of InAs quantum dash laser on InP(100) through optimizing double cap technique, *Appl. Phys. Lett.* 94, 081107 (2009).
29. V. Sichkovskyi, M. Waniczek, and J. Reithmaier, High-gain wavelength-stabilized 1.55 μm InAs/InP(100) based lasers with reduced number of quantum dot active layers, *Appl. Phys. Lett.* 102, 221117 (2013).
30. C. Paranthoën et al., Height dispersion control of InAs/InP(113)B quantum dots emitting at 1.55 μm, *Appl. Phys. Lett.* 78, 1751 (2001).
31. J. Kotani, P. J. van Veldhoven, T. de Vries, B. Smalbrugge, E. A. J. M. Bente, M. K. Smit, and R. Notzel, First demonstration of single-layer InAs/InP (100) quantum-dot laser: Continuous wave, room temperature, ground state, *Electron. Lett.* 45, 1317 (2009).
32. E. Homeyer, R. Piron, F. Grillot, O. Dehaese, K. Tavernier, E. Macé, A. Le Corre, and S. Loualiche, First demonstration of a 1.52 μm RT InAs/InP (311)B laser with an active zone based on a single QD layer, *Semicond. Sci. Technol.* 22, 827 (2007).
33. C. Cornet et al., Electronic and optical properties of InAs/InP quantum dots on InP(100) and InP(311)B substrates: Theory and experiment, *Phys. Rev. B* 74, 035312 (2006).
34. V. Ustinov, A. Zhukov, A. Y. Egorov, A. Kovsh, S. Zaitsev, and N. Y. Gordeev, Low threshold quantum dot injection laser emitting at 1.9 μm, *Electron. Lett.* 34, 670 (1998).
35. V. Ustinov, A. Kovsh, A. Zhukov, A. Y. Egorov, N. N. Ledentsov, and A. V. Lunev, Low-threshold quantum-dot injection heterolaser emitting at 1.84 μm, *Tech. Phys. Lett.* 24, 22 (1998).
36. K. Nishi, M. Yamada, T. Anan, A. Gomyo, and S. Sugou, Long-wavelength lasing from InAs self-assembled quantum dots on (311)B InP, *Appl. Phys. Lett.* 73, 526 (1998).

AQ10

37. N. Bertru et al., Two-dimensional ordering of self-assembled InAs quantum dots grown on (311)B InP substrate, in *Proceedings of SPIE, Quantum Sensing and Nanophotonic Devices VII*, Vol. 7608, p. 76081B (2010).
38. P. Miska, J. Even, C. Paranthoën, O. Dehaese, H. Folliot, S. Loualiche, M. Senes, and X. Marie, Optical properties and carrier dynamics of InAs/InP(113)B quantum dots emitting between 1.3 and 1.55 μm for laser applications, *Physica E* 17, 56 (2003).
39. C. Paranthoën et al., Growth and optical characterizations on InAs quantum dots on InP substrate: Toward 1.55 μm quantum dot laser, *J. Cryst. Growth* 251, 230 (2003).
40. P. Caroff, C. Paranthoen, C. Platz, O. Dehaese, H. Folliot, and N. Bertru, High-gain and low-threshold InAs quantum-dot lasers on InP, *Appl. Phys. Lett.* 87, 243107 (2005).
41. E. Homeyer, R. Piron, F. Grillot, O. Dehaese, K. Tavernier, and E. Macé, Demonstration of a low threshold current in 1.54 μm InAs/InP (311)B quantum dot laser with reduced quantum dot stacks, *Jpn. J. Appl. Phys.* 46, 6903 (2007).
42. K. Klaime, C. Clo, R. Piron, C. Paranthoen, D. Thiam, and T. Batte, 23 and 39 GHz low phase noise monosection InAs/InP (113)B quantum dots mode-locked lasers, *Opt. Express* 21, 29000 (2013).
43. H. Saito, K. Nishi, and S. Sugou, Ground-state lasing at room temperature in long-wavelength InAs quantum-dot lasers on InP(311)B substrates, *Appl. Phys. Lett.* 78, 267 (2001).

AQ11

44. K. Akahane, N. Yamamoto, and T. Kawanishi, Wavelength tunability of highly stacked quantum dot laser fabricated by a strain compensation technique, in *Proceedings of the 22nd IEEE International Semiconductor Laser Conference* (*ISLC*), Vol. 37 (2010).
45. K. Akahane, N. Yamamoto, and T. Kawanishi, The dependence of the characteristic temperature of highly stacked InAs quantum dot laser diodes fabricated using a strain-compensation technique on stacking layer number, in *Proceedings of the 22nd IEEE International Semiconductor Laser Conference* (*ISLC*), Vol. 82 (2012).
46. C. N. Allen, P. Poole, P. Barrios, P. Marshall, G. Pakulski, and S. Raymond, External cavity quantum dot tunable laser through 1.55 μm, *Physica E* 26, 372 (2005).

47. F. Lelarge, B. Rousseau, B. Dagens, F. Poingt, F. Pommereau, and A. Accard, Room temperature continuous-wave operation of buried ridge stripe lasers using InAs-InP(100) quantum dots as active core, *IEEE Photon. Technol. Lett.* 17, 1369 (2005).
48. S. Anantathanasarn et al., Lasing of wavelength-tunable (1.55 μm region) InAs/InGaAsP/InP (100) quantum dots grown by metal organic vapor-phase epitaxy, *Appl. Phys. Lett.* 89, 073115 (2006).
49. J. S. Kim, J. H. Lee, S. U. Hong, W. S. Han, H. S. Kwack, and C. W. Lee, Long-wavelength laser based on self-assembled InAs quantum dots in InAlGaAs on InP(001), *Appl. Phys. Lett.* 85, 1033 (2004).
50. J. S. Kim, J. H. Lee, S. U. Hong, W. S. Han, H. S. Kwack, and C. W. Lee, Room-temperature operation of InP-based quantum dot laser, *IEEE Photon. Technol. Lett.* 16, 1607 (2004).
51. C. Gilfert, V. Ivanov, N. Oehl, M. Yacob, and J. Reithmaier, High gain 1.55 μm diode lasers based on InAs quantum dot like active regions, *Appl. Phys. Lett.* 98, 201102 (2011).
52. O. Mollet, A. Martinez, K. Merghem, S. Joshi, J.-G. Provost, F. Lelarge, and A. Ramdane, Dynamic characteristics of undoped and p-doped Fabry-Perot InAs/InP quantum dash based ridge waveguide lasers for access/metro networks, *Appl. Phys. Lett.* 105, 141113 (2014).
53. C. Peucheret, *Direct and External Modulation of Light*, Technical University of Denmark, Kongens Lyngby, Denmark, 2009.
54. B. O. Seraphin and N. Bottka, Franz-Keldysh effect of the refractive index in semiconductors, *Phys. Rev.* 139, A560 (1965).
55. K. Kechaou, T. Anfray, K. Merghem, C. Aupetit-Berthelemot, G. Aubin, C. Kazmierski, C. Jany, P. Chanclou, and D. Erasme, Improved NRZ transmission distance at 20 Gbit/s using dual electro-absorption modulated laser, *Electron. Lett.* 48, 335 (2012).
56. D. Erasme et al., The dual-electroabsorption modulated laser, a flexible solution for amplified and dispersion uncompensated networks over standard fiber, *J. Lightwave Technol.* 32, 4068 (2014).
57. A. Martinez et al., Dynamic properties of InAs/InP(311B) quantum dot Fabry-Perot lasers emitting at 1.52-μm, *Appl. Phys. Lett.* 93, 021101 (2008).
58. D. Gready, G. Eisenstein, C. Gilfert, V. Ivanov, and J. P. Reithmaier, High-speed low-noise InAs/InAlGaAs/InP 1.55-μm quantum-dot lasers, *IEEE Photon. Technol. Lett.* 24, 809 (2012).
59. D. Gready, G. Eisenstein, V. Ivanov, C. Gilfert, F. Schnabel, A. Rippien, J. P. Reithmaier, and C. Bornholdt, High speed 1.55 μm InAs/InAlGaAs/InP quantum dot laser, *IEEE Photon. Technol. Lett.* 26, 11 (2014).
60. S. Bhowmick, M. Z. Baten, T. Frost, B. S. Ooi, and P. Bhattacharya, High performance InAs/In0.53Ga0.23Al0.24As/InP quantum dot 1.55 μm tunnel injection laser, *IEEE J. Quantum Electron.* 50, 7 (2014).
61. W. Kaiser, K. Mathwig, S. Deubert, J. P. Reithmaier, F. Forchel, O. Parillaud, M. Krakowski, D. Hadass, V. Mikhelashvili, and G. Eisenstein, Static and dynamic properties of laterally coupled DFB lasers based on InAs/InP Qdash structures, *Electron. Lett.* 41 (2005).
62. Z. Mi and P. Bhattacharya, DC and dynamic characteristics of p-doped and tunnel injection 1.65 μm InAs quantum-dash lasers grown on InP(001), *IEEE J. Quantum Electron.* 42, 1224 (2006).
63. S. Hein, V. von Hinten, W. Kaiser, S. Hofling, and A. Forchel, Dynamic properties of 1.5 μm quantum dash lasers on (100) InP, *Electron. Lett.* 43 (2007).
64. F. Lelarge et al., Recent advances on InAs/InP quantum dash based semiconductor lasers and optical amplifiers operating at 1.55 μm, *IEEE J. Sel. Top. Quantum Electron.* 13, 111 (2007).
65. Q. Zou, K. Merghem, S. Azouigui, A. Martinez, A. Accard, N. Chimot, F. Lelarge, and A. Ramdane, Feedback-resistant p-type doped InAs/InP quantum-dash distributed feedback lasers for isolator-free 10 Gb/s transmission at 1.55 μm, *Appl. Phys. Lett.* 97, 231115 (1010).
AQ12
66. N. Chimot, S. Joshi, G. Aubin, K. Merghem, S. barbet, A. Accard, A. Ramdane, and F. Lelarge, 1550 nm InAs/InP quantum dash based directly modulated lasers for next generation passive optical network, IEEE, p. 177 (2013).
67. S. Joshi, N. Chimot, L. A. Neto, A. Accard, and J. G. Provost, Quantum dash based directly modulated lasers for long-reach access networks, *Electron. Lett.* 50, 534 (2014).
68. R. S. Tucker, Green optical communications—Part I: Energy limitations in transport, *IEEE J. Sel. Top. Quantum Electron.* 17, 245 (2011).
69. D. Gready, G. Eisenstein, M. Gioannini, I. Montrosset, D. Arsenijevic, H. Schmeckebier, M. Stubenrauch, and D. Bimberg, On the relationship between small and large signal modulation capabilities in highly nonlinear quantum dot lasers, *Appl. Phys. Lett.* 102, 101107 (2013).
70. S. Joshi, N. Chimot, A. Ramdane, and F. Lelarge, On the nature of the linewidth enhancement factor in p-doped quantum dash based lasers, *Appl. Phys. Lett.* 105, 241117 (2014).

71. M. Gioannini and I. Montrosset, Numerical analysis of the frequency chirp in quantum-dot semiconductor lasers, *IEEE J. Quantum Electron.* 43, 941 (2007).
72. C. Cornet, C. Platz, P. Caroff, J. Even, C. Labbé, H. Folliot, and A. Le Corre, Approach to wetting-layer-assisted lateral coupling of InAs/InP quantum dots, *Phys. Rev. B* 72, 035342 (2005).
73. R. Heitz, F. Guffarth, K. Poetschke, A. Schliwa, D. Bimberg, N. D. Zakharov, and P. Werner, Shell-like formation of self-organized InAs/GaAs quantum dots, *Phys. Rev. B* 71, 045325 (2005).
74. A. J. Nozik, Multiple exciton generation in semiconductor quantum dots, *Chem. Phys. Lett.* 457, 3 (2008).
75. P. Miska, J. Even, O. Dehaese, and X. Marie, Carrier relaxation dynamics in InAs/InP quantum dots, *Appl. Phys. Lett.* 92, 191103 (2008).
76. K. Veselinov, F. Grillot, C. Cornet, J. Even, A. Bekiarski, M. Gioannini, and S. Loualiche, Analysis of the double laser emission occurring in 1.55-μm InAs-InP(113)B quantum-dot lasers, *IEEE J. Quantum Electron.* 43, 810 (2007).
77. R. Nagarajan, M. Ishikawa, T. Fukushima, R. Geels, and J. Bowers, High speed quantum well lasers and carrier transport effects, *IEEE J. Quantum Electron.* 28, 1990 (1992).
78. L. A. Coldren and S. W. Corzine, *Diode Lasers and Photonic Integrated Circuits*, New York: Wiley, 1995.
79. J. Siegert, S. Marcinkevicius, and Q. X. Zhao, Carrier dynamics in modulation-doped InAs/GaAs quantum dots, *Phys. Rev. B* 72, 085316 (2005).
80. S. Marcinkevicius and R. Leon, Carrier capture and escape in $In_xGa_{1-x}As$/GaAs quantum dots: Effects of intermixing, *Phys. Rev. B* 59, 4630 (1999).
81. T. R. Nielsen, P. Gartner, and F. Jahnke, Many-body theory of carrier capture and relaxation in semiconductor quantum-dot lasers, *Phys. Rev. B* 69, 235314 (2004).
82. B. Ohnesorge, M. Albrecht, J. Oshinowo, A. Forchel, and Y. Arakawa, Rapid carrier relaxation in self-assembled InxGa1-xAs/GaAs quantum dots, *Phys. Rev. B* 54, 11532 (1996).
83. I. V. Ignatiev, I. E. Kozin, S. V. Nair, H. W. Ren, S. Sugou, and Y. Masumoto, Carrier relaxation dynamics in InP quantum dots studied by artificial control of nonradiative losses, *Phys. Rev. B* 61, 15633 (2000).
84. M. Lorke, T. R. Nielsen, J. Seebeck, P. Gartner, and F. Jahnke, Influence of carrier-carrier and carrier-phonon correlations on optical absorption and gain in quantum-dot systems, *Phys. Rev. B* 73, 085324 (2006).
85. I. Magnusdottir, S. Bischoff, A. V. Uskov, and J. Mork, Geometry dependence of Auger carrier capture rates into cone-shaped self-assembled quantum dots, *Phys. Rev. B* 67, 205326 (2003).
86. U. Bockelmann and T. Egeler, Electron relaxation in quantum dots by means of Auger processes, *Phys. Rev. B* 46, 15574 (1992).
87. P. Ferreira and G. Bastard, Phonon assisted capture and intra-dot Auger relaxation in quantum dots, *Appl. Phys. Lett.* 74, 2818 (1999).
88. P. Miska, J. Even, X. Marie, and O. Dehaese, Electronic structure and carrier dynamics in InAs/InP double-cap quantum dots, *Appl. Phys. Lett.* 94, 061916 (2009).
89. A. V. Uskov, J. McInerney, F. Adler, H. Schweizer, and M. H. Pilkuhn, Auger carrier capture kinetics in self-assembled quantum dot structures, *Appl. Phys. Lett.* 72, 58 (1998).
90. A. V. Uskov, F. Adler, H. Schweizer, and M. H. Pilkuhn, Auger carrier relaxation in self-assembled quantum dots by collisions with two-dimensional carriers, *J. Appl. Phys.* 81, 7895 (1997).
91. W. W. Chow and S. W. Koch, Theory of semiconductor quantum-dot laser dynamics, *IEEE J. Quantum Electron.* 41, 495 (2005).
92. W. W. Chow and S. W. Koch, *Semiconductor-Laser Fundamentals*, Berlin, Germany: Springer, 1999.
93. T. W. Berg, S. Bischoff, I. Magnusdottir, and J. Mørk, Ultrafast gain recovery and modulation limitations in self-assembled quantum-dot devices, *IEEE Photon. Technol. Lett.* 13, 541 (2001).
94. W. W. Chow, M. Lorke, and F. Jahnke, Will quantum dots replace quantum wells as the active medium of choice in future semiconductor lasers, *IEEE J. Sel. Top. Quantum Electron.* 17, 1349 (2011).
95. T. Takahashi and Y. Arakawa, Nonlinear gain effects in quantum well, quantum well wire, and quantum well box lasers, *IEEE J. Quantum Electron.* 27, 1824 (1991).
96. M. Willatzen, A. Uskov, J. Mork, H. Olesen, B. Tromborg, and A. P. Jauho, Nonlinear gain suppression in semiconductor lasers due to carrier heating, *IEEE Photon. Technol. Lett.* 3, 606 (1991).
AQ13 97. D. J. Klotzkin, *Introduction to Semiconductor Lasers for Optical Communications*, Springer, 2014.
98. Y. Lam and J. Singh, Monte Carlo simulation of gain compression effects in GRINSCH quantum well laser structures, *IEEE J. Quantum Electron.* 30, 2435 (1994).

99. H. C. Schneider, W. W. Chow, and S. W. Koch, Anomalous carrier-induced dispersion in quantum-dot active media, *Phys. Rev. B* 66, 041310(R) (2002).
100. A. V. Uskov, E. P. O'Reilly, D. McPeake, N. N. Ledentsov, D. Bimberg, and G. Huyet, Carrier-induced refractive index in quantum dot structures due to transitions from discrete quantum dot levels to continuum states, *Appl. Phys. Lett.* 84, 272 (2004).
101. S. P. Hegarty, B. Corbett, J. G. McInerney, and G. Huyet, Free-carrier effect on index change in 1.3 μm quantum-dot lasers, *Electron. Lett.* 41, 416 (2005).
102. M. Osiński and J. Buus, Linewidth broadening factor in semiconductor lasers—An overview, *IEEE J. Quantum Electron.* QE-23, 9 (1987).
103. G. H. Duan, P. Gallion, and G. Debarge, Analysis of the phase-amplitude coupling factor and spectral linewidth of distributed feedback and composite-cavity semiconductor lasers, *IEEE J. Quantum Electron.* 26, 32 (1990).
104. G. Duan, P. Gallion, and G. Gebarge, Analysis of frequency chirping of semiconductor lasers in presence of optical feedback, *Opt. Lett.* 12, 800 (1987).
105. G. P. Agrawal, Intensity dependence of the linewidth enhancement factor and its implications for semiconductor lasers, *IEEE Photon. Technol. Lett.* 1, 212 (1989).
106. S. Wieczorek, B. Krauskopf, and D. Lenstra, Multipulse excitability in a semiconductor laser with optical injection, *Phys. Rev. Lett.* 88, 063901 (2002).
107. B. Haegeman, K. Engelborghs, D. Roose, D. Pierous, and T. Erneux, Stability and rupture of bifurcation bridges in semiconductor lasers subject to optical feedback, *Phys. Rev. E* 66, 046216 (2002).
108. M. Sciamanna, P. Mégret, and M. Blondel, Hopft bifurcation cascade in small-α laser diodes subject to optical feedback, *Phys. Rev. E* 69, 046209 (2004).
109. K. Panajotov, M. Sciamanna, M. Arteaga, and H. Thienpont, Optical feedback in vertical-cavity surface-emitting lasers, *IEEE J. Sel. Top. Quantum Electron.* 19, 1700312 (2012).
110. T. C. Newell, D. J. Bossert, A. Stintz, B. Fuchs, K. J. Malloy, and L. F. Lester, Gain and linewidth enhancement factor in InAs quantum-dot laser diodes, *IEEE Photon. Technol. Lett.* 11, 1527(1999).
111. Z. Mi, P. Bhattacharya, and S. Fathpour, High-speed 1.3 μm tunnel injection quantum-dot lasers, *Appl. Phys. Lett.* 86, 153109 (2005).
112. B. Dagens, A. Markus, J. X. Chen, J. G. Provost, D. Make, O. Le Goueziou, J. Landreau, A. Foire, and B. Thedrez, Gaint linewidth enhancement factor and purely frequency modulated emission from quantum dot laser, *Electron. Lett.* 41, 323 (2005).
113. F. Grillot, K. Veselinov, M. Gioannini, I. Montrosset, J. Even, R. Piron, E. Homeyer, and S. Loualiche, Spectral analysis of 1.55 μm InAs–InP(113)B quantum-dot lasers based on a multipopulation rate equations model, *IEEE J. Quantum Electron.* 45, 872 (2009).
114. C. Wang, F. Grillot, and J. Even, Impacts of wetting layer and excited state on the modulation response of quantum-dot lasers, *IEEE J. Quantum Electron.* 48, 1144 (2012).
115. M. Kuntz, Modulated InGaAs/GaAs quantum dot lasers, PhD thesis, Berlin, Germany, 2006.
116. N. A. Naderi, External control of semiconductor nanostructure lasers, PhD thesis, University of New Mexico, Albuquerque, NM, 2011.
117. A. E. Zhukov, M. V. Maximov, A. V. Savelyev, Yu. M. Shernyakov, F. I. Zubov, V. V. Korenev, A. Martinez, A. Ramdane, J.-G. Provost, and D. A. Livshits, Gain compression and its dependence on output power in quantum dot lasers, *J. Appl. Phys.* 113, 233103 (2013).
118. J. Oksanen and J. Tulkki, Linewidth enhancement factor and chirp in quantum dot lasers, *J. Appl. Phys.* 94, 1983 (2003).
119. S. Melnik, G. Huyet, and A. V. Uskov, The linewidth enhancement factor α of quantum dot semiconductor lasers, *Opt. Express* 14, 2950 (2006).
120. S. Wieczorek, B. Krauskopf, T. B. Simpson, and D. Lenstra, The dynamical complexity of optically injected semiconductor lasers, *Phys. Rep.* 416, 1 (2005).
121. W. W. Chow and F. Jahnke, On the physics of semiconductor quantum dots for applications in lasers and quantum optics, *Prog. Quantum Electron.* (2013).
122. A. Markus, J. X. Chen, O. Gauthier-Lafaye, J. G. Provost, C. Paranthoen, and A. Fiore, Impact of intraband relaxation on the performance of a quantum-dot laser, *IEEE J. Sel. Top. Quantum Electron.* 9, 1308 (2003).
123. B. Lingnau, W. W. Chow, E. Schöll, and K. Lüdge, Feedback and injection locking instabilities in quantum-dot lasers: A microscopically based bifurcation analysis, *New J. Phys.* 15, 093031 (2013).

124. F. Grillot, B. Dagens, J. G. Provost, H. Su, and L. F. Lester, Gain compression and above-threshold linewidth enhancement factor in 1.3 µm InAs-GaAs quantum-dot lasers, *IEEE J. Quantum Electron.* 44, 946 (2008).
125. J.-G. Provost and F. Grillot, Measuring the chirp and the linewidth enhancement factor of optoelectronic devices with a Mach-Zehnder interferometer, *IEEE Photon. J.* 3, 476 (2011).
126. C. Cornet, C. Labbé, H. Folliot, N. Bertru, O. Dehaese, J. Even, A. Le Corre, C. Paranthoën, C. Platz, and S. Loualiche, Quantitative investigations of optical absorption in InAs/InP (311)B quantum dots emitting at 1.55 µm wavelength, *Appl. Phys. Lett.* 85, 5685 (2004).
127. Z. Mi and P. Bhattacharya, Analysis of the linewidth-enhancement factor of long-wavelength tunnel-injection quantum-dot lasers, *IEEE J. Quantum Electron.* 43, 363 (2007).
128. C. Wang, M. Osiński, J. Even, and F. Grillot, Phase-amplitude coupling characteristics in directly modulated quantum dot lasers, *Appl. Phys. Lett.* 105, 221114 (2014).
129. S. Gerhard, C. Schilling, F. Gerschutz, M. Fischer, J. Koeth, I. Krestnikov, A. Kovsh, M. Kamp, S. Hofling, and A. Forchel, Frequency-dependent linewidth enhancement factor of quantum-dot lasers, *IEEE Photon. Technol. Lett.* 20, 1736 (2008).
130. K. Lüdge and H. G. Schuster, *Nonlinear Laser Dynamics: From Quantum Dots to Cryptography*, New York: Wiley, 2011.
131. B. Lingnau, K. Lüdge, W. W. Chow, and E. Schöll, Influencing modulation properties of quantum-dot semiconductor lasers by carrier lifetime engineering, *Appl. Phys. Lett.* 101, 131107 (2012).
132. C. Wang, B. Lingnau, K. Lüdge, J. Even, and F. Grillot, Enhanced dynamic performance of quantum dot semiconductor lasers operating on the excited state, *IEEE J. Quantum Electron.* 50, 723 (2014).
AQ14 133. T. B. Simpon, J. M. Liu, and A. Gavrielides, Bandwidth enhancement and broadband noise reduction in injection-locked semiconductor lasers, *IEEE Photon. Technol. Lett.* 7, 709 (1995).
134. A. Murakami, K. Kawashima, and K. Atsuki, Cavity resonance shift and bandwidth enhancement in semiconductor lasers with strong light injection, *IEEE J. Quantum Electron.* 39, 1196 (2003).
135. F. Grillot, C. Wang, N. A. Naderi, and J. Even, Modulation properties of self-injected quantum-dot semiconductor diode lasers, *IEEE J. Sel. Top. Quantum Electron.* 19, 1900812 (2013).
136. J.-P. Zhuang and S.-C. Chan, Phase noise characteristics of microwave signals generated by semiconductor laser dynamics, *Opt. Express* 23, 2777 (2015).

AUTHOR QUERIES

[AQ1] Running head has been edited from the Chapter title. Please check if it is okay.
[AQ2] Please check if edit to the sections heading is okay.
[AQ3] Please check if the cross reference to Figure 3.5 in the sentence “This simplified picture...” should be changed to Figure 3.6 as per the text.
[AQ4] The citations “Figure 3.1” in the paragraph “Figure 3.6 shows the schematic of...” have been changed to Figure 3.6. Please check.
[AQ5] Both “ τ_p ” and “τ_P” have been used in the chapter. Please check and make one form consistent.
[AQ6] Both “Γ_P” and “ Γ_p” have been used for representing “optical confinement factor”. Please check and make one form consistent.
[AQ7] Please provide publisher and editor(s) details for Ref. [13].
[AQ8] Please provide volume number and page range for Refs. [25,121].
[AQ9] As Refs. [27] and [37] are the same, the repeated entry has been deleted. Please check if okay.
[AQ10] Please provide proceedings location for Ref. [37] and also update in the source line of Figure 3.1.
[AQ11] Please provide proceedings location for Refs. [44,45].
[AQ12] Please provide proceedings title and location for Ref. [66].
[AQ13] Please provide publisher location for Ref. [97].
[AQ14] Please check if edit made to the author group of Ref. [133] is correct.